2

Electron Acceleration Using an Ultrashort Ultraintense Laser Pulse

Eisuke Miura
National Institute of Advanced Industrial Science and Technology (AIST)
Tsukuba central 2, 1-1-4 Umezono, Tsukuba, Ibaraki
Japan

1. Introduction

With recent progress in ultrashort ultraintense laser technologies such as chirped pulse amplification (CPA) (Strickland & Mourou, 1985), the peak power of a laser pulse is increasing year by year, and the focused intensity of 10^{21} W/cm^2 has been achieved (Aoyama et al., 2003; Perry et al., 1999). When the focused intensity of a laser pulse is higher than 10^{18} W/cm^2, quiver velocity of an electron is close to the speed of light in such a high electromagnetic field. Various nonlinear phenomena are caused by the relativistic effect of the electron motion. Self-focusing, higher harmonic generation, and so on, which are well-known phenomena in nonlinear optics, have been observed in laser-plasma interactions.

An ultrashort ultraintense laser pulse propagating in a plasma can excite a plasma wave by the nonlinear force of a high electromagnetic field, called the ponderomotive force. A longitudinal electric field is formed by the plasma wave, and electrons trapped in the potential of the plasma wave can be accelerated. This is the concept of laser-driven plasma-based electron acceleration (LPA) (Tajima & Dawson, 1979). The longitudinal accelerating electric field of the plasma wave is higher than 100 GV/m, which is a thousand times higher than that of present radio-frequency (rf) accelerators. Such a high accelerating field enables us to realize compact electron accelerators and/or obtain extremely high energy electrons. Furthermore, the electron pulse duration is extremely short, of the order of tens of femtoseconds, because the wavelength of the accelerating field, that is the plasma wave, is of the order of tens of micrometers. Next-generation electron accelerators with such unique characteristics will be realized using LPA.

Since the concept was proposed, various experimental and theoretical studies have been conducted (Esarey et al., 2009; 1996). Pioneering works of the proof-of-principle such as generation of a high accelerating field and energetic electron beams have been so far presented (Joshi et al., 1984; Kitagawa et al., 1992; Malka et al., 2002; Modena et al., 1995; Nakajima et al., 1995). However, the energy spectra of the electron beams were Maxwell-like distributions, and the beam qualities were far from those required for various applications. In 2004, a major breakthrough was brought about with the generation of well-collimated electron beams with a narrow energy spread, that is quasi-monoenergetic electron (QME) beams (Faure et al., 2004; Geddes et al., 2004; Mangles et al., 2004; Miura et al., 2005). This result is a significant step toward the realization of a laser electron accelerator.

In this chapter, we provide the overview of the present status of research on LPA. First, we briefly describe the principle of LPA. Second, we present recent results of works conducted at the National Institute of Advanced Industrial Science and Technology (AIST). Generation of QME beams is mainly presented. We also present particle-in-cell simulations to discuss the mechanism and the conditions of QME beam generation. Using a femtosecond electron pulse obtained by LPA, a compact, all-optical, ultrashort X-ray source can be realized on the basis of laser Compton scattering. Third, we present X-ray generation by laser Compton scattering using a laser-accelerated electron beam. Finally, we briefly review recent progress toward a next step and future prospects.

2. Principle of laser-driven plasma-based electron acceleration

2.1 Electron motion in a electromagnetic field

Let us consider an electron motion in a electromagnetic field. The equation of motion for a free electron of charge e in an electromagnetic (laser) field is given by the Lorentz equation

$$\frac{d\mathbf{p}}{dt} = -e(\mathbf{E} + \mathbf{v} \times \mathbf{B}) \,, \tag{1}$$

where $\mathbf{p}$=$\gamma m_e \mathbf{v}$, $\mathbf{v}$, $\mathbf{E}$, and $\mathbf{B}$ are the momentum and velocity of an electron, and the electric and magnetic field, respectively. Here, m_e and γ are the electron mass and the relativistic Lorentz factor. In the case of a weak electromagnetic field, $\mathbf{v} \times \mathbf{B}$ component is negligible, and Eq. 1 is simplified to $m_e \frac{d\mathbf{v}}{dt} = -e\mathbf{E}$. For a linearly polarized laser field, the electron quiver velocity v_q is given by $v_q = eE_L / m_e \omega_L$, where E_L and ω_L are the amplitude and frequency of the laser field. The ratio of the electron quiver velocity to the speed of light c is defined by

$$a_0 = \frac{eE_L}{m_e \omega_L c} = 8.5 \times 10^{-10} \lambda_L[\mu\text{m}] \sqrt{(I_L[\text{W/cm}^2])} \,, \tag{2}$$

where λ_L and I_L are the laser wavelength and intensity. This gives an expression for the normalized vector potential a_0. Relativistic effects are brought about in an electron motion in a laser field yielding $a_0 \geq 1$. This region is called relativistic region. For example, the intensity of 2.2×10^{18} W/cm^2 gives $a_0 = 1$ for 800-nm laser light.

By averaging $\frac{1}{2} m_e {v_q}^2$ over one oscillation period of a field, the electron quiver energy is defined by

$$U_P[\text{eV}] = \frac{1}{2} m_e \langle {v_q}^2 \rangle = \frac{e^2 {E_L}^2}{4 m_e {\omega_L}^2} = 9.3 \times 10^{-14} (\lambda_L[\mu\text{m}])^2 I_L[\text{W/cm}^2] \,. \tag{3}$$

This is an expression for the ponderomotive potential U_P. The ponderomotive potential results in a force $\mathbf{F_P}$=$-\nabla U_P$, that is the ponderomotive force. The ponderomotive force is directed along the intensity gradient of a laser pulse envelope, and perpendicular to the laser propagation direction. The force pushes electrons out of the region of the laser pulse, and becomes the driving force for exciting a plasma wave in a plasma.

2.2 Excitation of plasma wave

Let us consider the propagation of an ultrashort ultraintense laser pulse in a low density plasma. The electron density of the plasma is much lower than the critical density n_c given by $n_c = \varepsilon_0 m_e {\omega_L}^2 / e^2$, where ε_0 is the vacuum permittivity. Electrons in the plasma are pushed out of the region of the laser pulse and separated from ions by the ponderomotive force. A local charge separation is formed, because it is regarded that ions are at rest in the short time close to the laser pulse duration. After some time, the laser pulse overtakes electrons pushed out and the space charge force starts to pull the electrons back. In turn, the charge excess is formed by the electrons pulled back near the laser propagation axis. The electrons are pushed out again. By the repetition of this process, plasma oscillation is driven. The plasma frequency ω_p for the electron density n_e is given by

$$\omega_p = \sqrt{\frac{e^2 n_e}{\varepsilon_0 m_e}} \, . \tag{4}$$

Because the plasma oscillation is driven together with the propagation of the laser pulse, the phase velocity of the plasma wave v_p is equal to the group velocity of the laser pulse given by

$$v_p = c\sqrt{1 - \frac{n_e}{n_c}} \, . \tag{5}$$

Electrons trapped in the plasma wave can be accelerated almost to the speed of light, because the phase velocity of the plasma wave is close to the speed of light in an underdense plasma ($n_e \ll n_c$).
In the linear region, a longitudinal electric field of a plasma wave E_x is give by

$$E_x = \delta n \frac{m_e \omega_p c}{e} \, , \tag{6}$$

where δn is the modulation of the electron density. For example, assuming $n_e = 10^{19}$ cm^{-3} and $\delta n = 0.3$, the electric field is 100 GV/m, corresponding to more than a thousand times as accelerating fields of present rf accelerators.
To explain the principle of LPA, typical particle-in-cell (PIC) simulation results are shown in Fig. 1. The initial electron density of a plasma is 1.7×10^{19} cm^{-3}, and the laser intensity of 800-nm light corresponds to the normalized vector potential of 5. A laser pulse propagates along the $x-$axis and is polarized along the $y-$axis. The snapshots of electron density distribution (a) and (b), the distributions of the electric field along the $y-$axis corresponding to the laser field (c) and (d), and the distributions of the electron density (solid curve) and the electric field (dashed curve) along the $x-$axis (e) and (f) are shown for different laser propagation lengths. As shown in Figs. 1(a) and (e), the period of the low-density and high-density parts is formed behind the laser pulse along the propagation axis, and a plasma wave is excited. As shown in Fig. 1(e), the peak longitudinal field along the $x-$axis, that is the accelerating field in LPA, reaches 700 GV/m.
The situation, in which a laser pulse drives a plasma wave behind itself, is similar to that in which a boat drives a wake on a sea. Then, LPA is also called laser wakefield acceleration (LFWA).

2.3 Trapping and acceleration of electrons

As described above, because the phase velocity of the plasma wave is close to the speed of light, the velocity of electrons should be also close to the speed of light for trapping into a plasma wave. To feed accelerated electrons, an electron gun was used as an external electron source (Amiranoff et al., 1995; Clayton et al., 1993; Ebrahim, 1994). In some experiments, hot electrons produced from a laser-irradiated solid target were used (Mori, Sentoku, Kondo, Tsuji, Nakanii, Fukumochi, Kashihara, Kimura, Takeda, Tanaka, Norimatsu, Tanimoto, Nakamura, Tampo, Kodama, Miura, Mima & Kitagawa, 2009; Nakajima et al., 1995). However, it has been demonstrated that electrons in a plasma can be almost

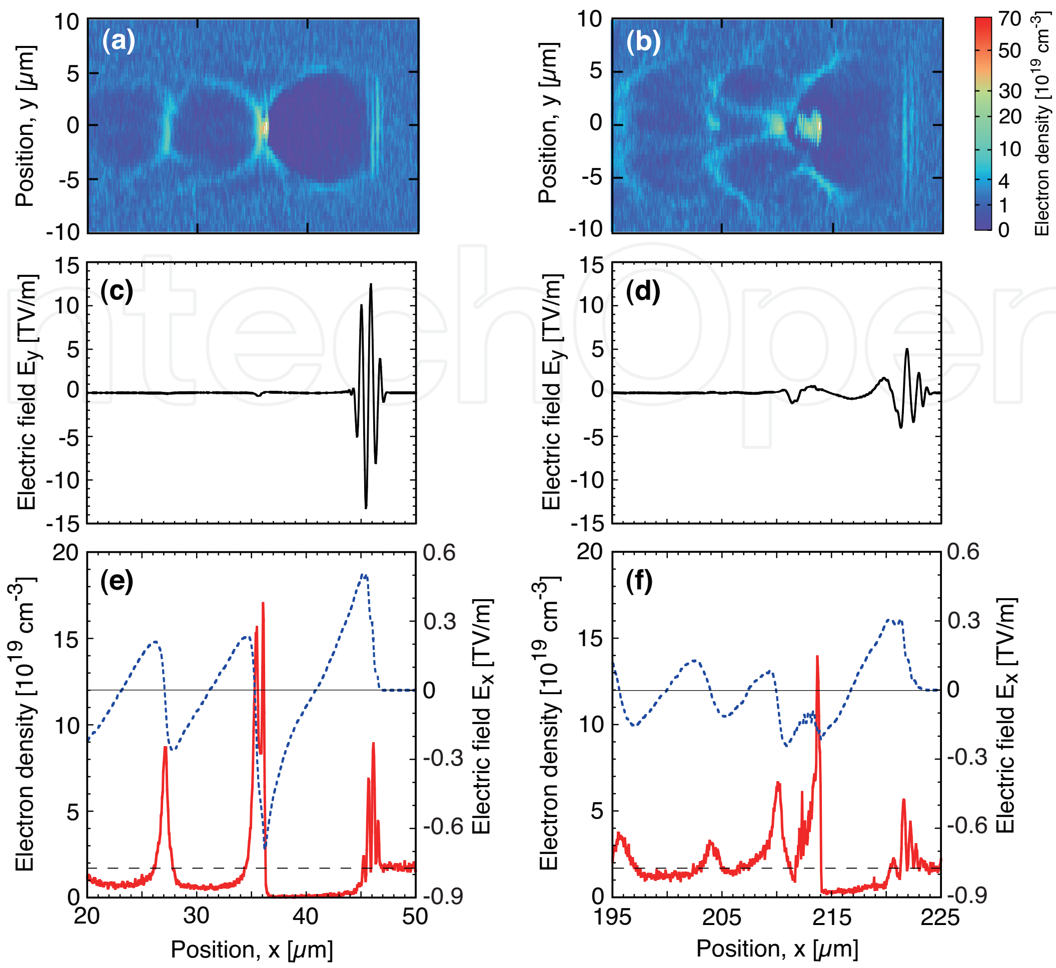

Fig. 1. Typical simulation results to explain the principle of LPA. Snapshots of electron density distribution on the $x - y$ plain (a) and (b), the distributions of the electric field along the $y-$axis corresponding to the laser field (c) and (d), and the distributions of the electron density (solid curve) and the electric field (dashed curve) corresponding to the accelerating field along the $x-$axis (e) and (f) are shown for different laser propagation lengths.

automatically injected and trapped into a plasma wave. This scheme is called self-injection scheme or self-trapping scheme. In the self-injection scheme, wave-breaking plays an important role (Bulanov et al., 1997; Decker et al., 1994). As shown in Fig. 1(e), a plasma wave with a large amplitude is excited, and the steeping of the wave occurs. As the laser pulse propagates further, the amplitude of the plasma wave becomes larger, and the wave finally breaks. This phenomenon is seen as whitecaps at the ocean. Electrons slip from the wave and are trapped into the plasma wave. As shown in Figs. 1(b) and (f), electrons are trapped and accelerated in the first period of the plasma wave and form an electron bunch.

The plasma wavelength $\lambda_p = 2\pi c/\omega_p$, which is the wavelength of the accelerating field, is the order of tens of micrometers. In the case shown in Fig. 1, the plasma wavelength is $\sim 10\ \mu$m. Electrons are trapped in the narrow region of the acceleration phase and the length of the electron bunch is a few micrometers as shown in Fig. 1(f). This electron bunch is regarded as an ultrashort electron pulse with a duration of tens of femtoseconds. Thus, a femtosecond electron pulse can be obtained by LPA.

The energy gain W_{max} is simply given by the product of the accelerating field and the acceleration length. In the linear region, the accelerating field is given by Eq. 6. The acceleration length is mainly limited by dephasing (phase slippage) of electrons trapped in a plasma wave. The dephasing is brought about by the difference between the phase velocity of a plasma wave and the velocity of accelerated electrons. Accelerated electrons in a plasma wave outrun the acceleration phase of the plasma wave, and enter the deceleration phase. In the linear region, the dephasing length L_d is given by

$$L_d = \frac{c\lambda_p/2}{c - v_p} \simeq \frac{n_c}{n_e}\lambda_p \, . \tag{7}$$

Then, the maximum energy gain is given by

$$W_{max} = 4m_e c^2 \frac{n_c}{n_e} \, . \tag{8}$$

For example, when the laser wavelength is 800 nm and the electron density is 10^{19} cm^{-3}, the dephasing length and the maximum energy gain are 1.8 mm and 350 MeV. In other words, electrons with an energy of 350 MeV can be accelerated in only 1.8-mm length.

The acceleration length is also limited by the diffraction of a laser beam and/or the energy depletion of a laser pulse for driving a plasma wave. The limit of the laser propagation length by the diffraction is not serious, because it is possible to achieve a longer propagation length by guiding a laser pulse using relativistic self-focusing, a capillary discharge plasma and so on. If the pump depletion length is defined as the length in consuming half of the initial laser pulse energy for driving a plasma wave, the pump depletion length is comparable to the dephasing length (Esarey et al., 1996). Then, the limit of the acceleration length by dephasing is dominant.

The description in this section is concentrated in the liner region. However, as shown in Fig. 1, most of phenomena in LPA are in the nonlinear region, and the treatment is important. The overview of analytical description in the nonlinear region has been provided in detailed review reports (Esarey et al., 2009; 1996).

2.4 Generation of quasi-monoenergetic electron beam with a narrow energy spread

Since the middle of 1990's, the generation of energetic electron beams based on a self-injection scheme has been demonstrated (Modena et al., 1995; Nakajima et al., 1995; Umstadter, Chen, Maksimchuk, Mourou & Wagner, 1996). Although collimated electron beams were generated, the energy spectra of the electron beams were Maxwell-like distributions and the energy spreads were large. These experiments were based on self-modulated laser wakefield acceleration (SM-LWFA) using a laser pulse with a picosecond duration and a high-density plasma with an electron density close to 10^{20} cm^{-3}. In such cases, the laser pulse length is longer than the plasma wavelength. The plasma wave with a large amplitude is excited via Raman scattering and/or the self-modulation instability and can accelerate trapped electrons. Heating the plasma occurs, when the plasma wave grows. In addition, the trapped electrons in the plasma wave interact with the laser field and can be also accelerated by the laser field directly, that is so-called direct laser acceleration (DLA) (Gahn et al., 1999). The combination of these electron acceleration mechanisms can lead to the broad electron energy spectrum.

However, in 2004, the generation of QME beams with a narrow energy spread was demonstrated by four groups (Faure et al., 2004; Geddes et al., 2004; Mangles et al., 2004; Miura et al., 2005). After that, many groups have so far reported the generation of QME beams (Hidding et al., 2006; Hosokai, Kinoshita, Ohkubo, Maekawa, Uesaka, Zhidkov, Yamazaki, Kotaki, Kando, Nakajima, Bulanov, Tomassini, Giulietti & Giulietti, 2006; Hsieh et al., 2006; Maksimchuk et al., 2007; Mori et al., 2006; Yamazaki et al., 2005). Most experimental results on QME beam generation have been explained by the acceleration in the highly nonlinear broken-wave regime, that is so-called bubble acceleration regime (Pukhov & Meyer-ter Vehn, 2002). In simulation results shown in Fig. 1, the conditions are close to those of the bubble acceleration regime. When an ultraintense laser pulse propagates in a plasma, it undergoes the self-focusing and the longitudinal pulse compression. Such laser pulse drives a highly nonlinear plasma wave and expels a large amount of electrons. Then, the electron cavitated region (bubble) is formed behind the laser pulse. The radially expelled electrons move along the boundary of the bubble and collide at the rear vertex of the bubble. Transverse wave-breaking (Bulanov et al., 1997) occurs and a large amount of electrons is injected into the bubble at the rear vertex. The field produced by the injected electrons terminates further electron injection. Electrons are trapped at the fixed narrow phase of the accelerating field. Thus, the QME beam with a narrow energy spread can be obtained. Because a large amount of electrons is instantaneously injected, the QME beam with high charge can be obtained. The electrons trapped near the rear vertex of the bubble are located behind the laser pulse. Because the trapped electrons are free from the laser pulse, an electron beam with low emittance can be obtained. These phenomena have been thoroughly investigated by many theoretical and numerical studies (Geissler et al., 2006; Gordienko & Pukhov, 2005; Kostyukov et al., 2004; Lu et al., 2007). For such bubble formation, one of the required conditions is that the spatially transverse and longitudinal sizes of the laser pulse match the plasma wavelength. To satisfy this condition, the experiments have been conducted using a focusing mirror with the long focal length yielding the spot size of $\sim 10\ \mu$m and an ultraintense laser pulse with a few tens of femtoseconds yielding the pulse length of $\sim 10\ \mu$m for a low density plasma around or less than 10^{19} cm^{-3} yielding the plasma wavelength of $\sim 10\ \mu$m.

3. Experimental and numerical studies on laser-driven plasma-based electron acceleration

In this section, recent results of works conducted in the National Institute of Advanced Industrial Science and Technology (AIST) (Masuda & Miura, 2008; Miura & Masuda, 2009) are presented as an example of experimental and numerical studies on LPA.

3.1 Experimental conditions

Laser system

A Ti:sapphire laser system with a repetition rate of 10 Hz based on CPA method was used for experiments. In our laser system, two intense laser pulses were available. A 20-fs laser pulse from a Kerr-lens mode-locked oscillator was stretched to 400 ps through an Öffner type pulse stretcher, which was an aberration-free type stretcher(Cheriaux et al., 1996). To control a laser pulse shape, an acousto-optic programmable dispersive filter (Dazzler: Fastlite)(Verluise et al., 2000) was installed after the pulse stretcher. The laser pulse was amplified by a regenerative amplifier and multi-pass amplifiers. To suppress and control a prepulse, a pulse cleaner composed of a Pockels cell and a thin film polarizer was set between the regenerative and the first muti-pass amplifiers. After the first multi-pass amplifier, the laser pulse was split into three pulses. The first pulse referred as main laser pulse was amplified by a multi-pass amplifier, and a laser pulse with an energy of 750 mJ, a pulse duration of 35-50 fs, and a center wavelength of 800 nm was obtained after a vacuum pulse compressor. The main laser pulse was used for electron acceleration. The second pulse referred as colliding laser pulse was amplified by two multi-pass amplifiers, and a laser pulse with an energy of 150 mJ, a pulse duration of 60 fs, and a center wavelength of 800 nm was obtained after a vacuum pulse compressor. Due to the priority to optimize a pulse shape of a main laser pulse, the spectrum control of a colliding laser pulse was not sufficient. Then, the pulse duration of the colliding laser pulse was little bit longer than that of the main laser pulse. The colliding laser pulse was used for X-ray generation by laser Compton scattering shown in Sec. 4. The third pulse referred as probe laser pulse with an energy of 0.5 mJ, a pulse duration of 60 fs, and a center wavelength of 800 nm was used for plasma diagnostics such as shadowgraph and interferogram.

Experiment setup

The experimental setup for electron acceleration is shown in Fig. 2. A p-polarized main laser pulse (400 mJ, 50 fs, 800 nm) was focused onto the edge of a helium gas jet using an $f/6$ off-axis parabolic mirror with a focal length of 300 mm. The laser spot size in vacuum was 9 μm at the full-width-at-half-maximum (FWHM), and the Rayleigh length was 230 μm. The energy concentration within the e^{-2} spot was 58% of the total laser energy. The peak intensity was 5.8×10^{18} W/cm^2, corresponding to the normalized vector potential of 1.6. The helium gas jet was ejected from a supersonic nozzle with a conical shape driven by a pulsed valve. The focal position was set at 1 mm above the nozzle exit. The diameter of the nozzle exit was 0.7 mm and the Mach number was 5.3. The density profile of the gas jet was measured with a Jamin interferometer. The density at the center was $\sim 5 \times 10^{18}$ cm^{-3}, corresponding to the electron density of $\sim 10^{19}$ cm^{-3}.

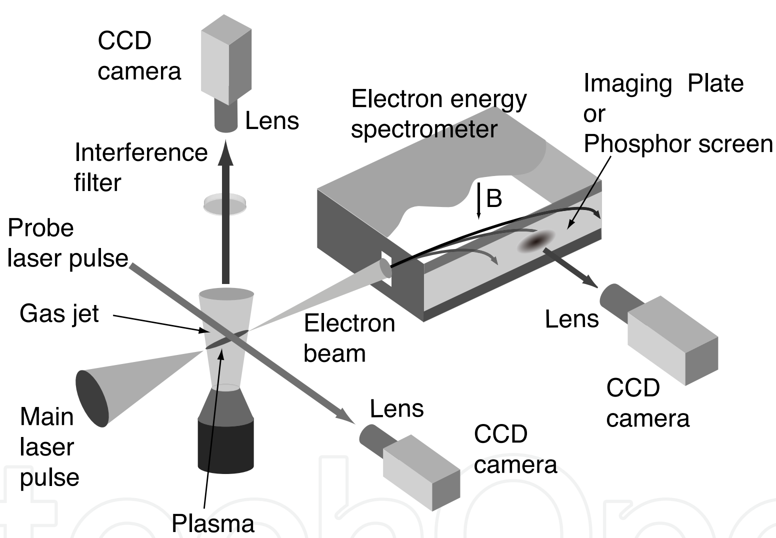

Fig. 2. Experimental setup for electron acceleration.

The energy spectrum of an electron beam was measured by an electron energy spectrometer with a dipole magnet. The measured energy range was from 1 to 80 MeV. An energy-resolved electron image was recorded on an imaging plate [(IP), Fujifilm: BAS-SR]. To estimate the absolute charge of electrons , the sensitivity curve reported in Ref.(Tanaka et al., 2005) was used. In addition, we have developed an absolutely-calibrated in-situ observation system for the electron energy spectrum. A $Gd_2O_2S:Tb$ phosphor screen (Mitsubishi chemical: DRZ-HIGH) coupled with a CCD camera was used as an electron detector. The sensitivity of the detection system was calibrated using an IP as the reference detector (Masuda et al., 2008). The absolute electron energy spectrum was in-situ observed with a single shot at a repetition rate of 1 Hz.

To observe the propagation of a laser pulse and the formation of a preformed plasma, a side-scattered light image and a shadowgraph image were observed simultaneously with the measurement of an electron energy spectrum. The side-scattered light image was observed through an interference filter of 800 nm from the top of the gas jet. The shadowgraph image was observed with a 60-fs, 800-nm probe laser pulse. The spatial resolutions in both the measurements were approximately 40 μm.
Contrast ratios of femtosecond prepulses, generated in a regenerative amplifier, preceding the main pulse by more than 4 ns were always kept to be less than 10^{-6} using a pulse cleaner. Our another work has demonstrated that the number of accelerated electrons was dramatically decreased for low contrast ratios of the femtosecond prepulses, although the laser power and the electron density of the plasma were different from those for the present experiment (Masuda & Miura, 2010). Then, the femtosecond prepulses were suppressed.

3.2 Quasi-monoenergetic electron beam generation

Figure 3(a) shows an energy-resolved electron image of a typical QME beam from a plasma with an electron density of 1.6×10^{19} cm^{-3} produced by an 8.3-TW laser pulse. The image was recorded on an IP with a single shot. The small spot indicates the generation of the monoenergetic beam with a narrow energy spread and a small divergence angle. The divergence angle in the vertical direction was estimated to be 7 mrad at the FWHM from the vertical size of the spot. The electron energy spectrum is shown in Fig. 3(b). A monoenergetic peak was observed at the energy of 38 MeV with the relative energy spread of 19%. Here, the relative energy spread is defined as the ratio of the energy spread at the FWHM to the peak energy. The observed energy spread was little bit larger than the instrumental resolution of several percent. The total number of electrons in the monoenergetic peak was 3.1×10^{8}, corresponding to the charge of 50 pC.
Figure 4 shows the electron energy spectra obtained by sequential 14 shots under the same conditions as those giving the result shown in Fig. 3. All the spectra were obtained with a single shot. To evaluate the stability of QME beam generation, the criterion values of principal

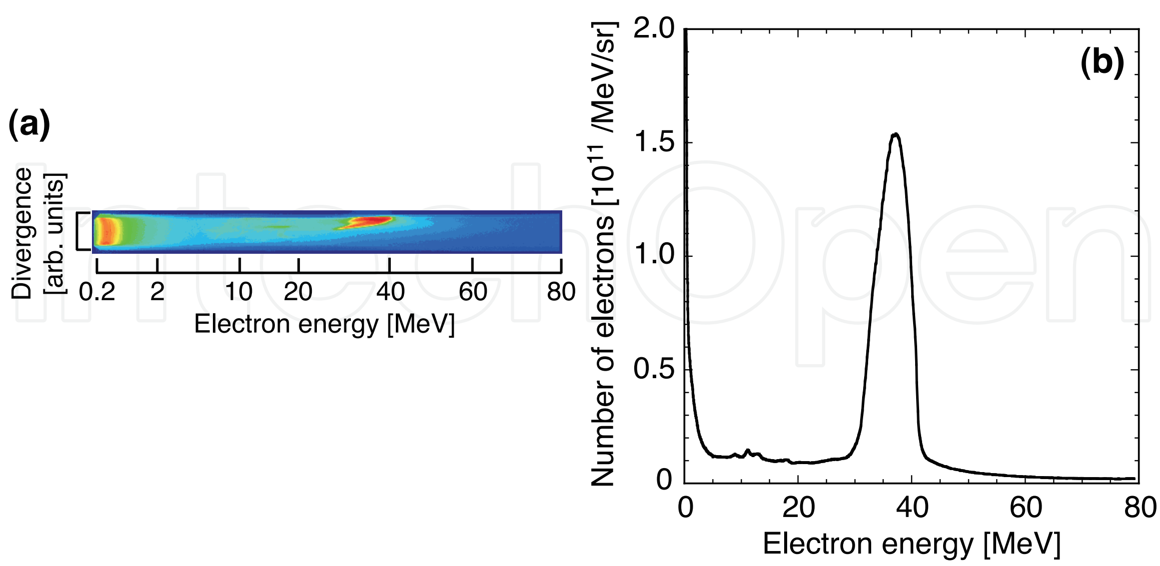

Fig. 3. (a) Typical energy-resolved electron image recorded on an IP with a single shot and (b) electron energy spectrum of a QME beam obtained from a plasma with an electron density of 1.6×10^{19} cm^{-3} produced by an 8.3-TW laser pulse.

beam parameters should be defined for judging QME beam generation. We set the following four criterion values. First, the peak energy is higher than 10 MeV. Second, the number of electrons in the electron energy spectrum is higher than 10^{10} /MeV/sr at the monoenergetic peak. Third, the ratio of the peak to the background at the monoenergetic peak is higher than 2. Forth, the relative energy spread is less than 50%. When all of these conditions are fulfilled, we consider that a QME beam has generated. According to the criteria, QME beams are obtained in 10 shots among 14 shots in the case of Fig. 4. The probability of QME beam generation is 70%, if the shot-to-shot fluctuations of the peak energy, the number of electrons, and so on are ignored. In our previous experiment (Masuda et al., 2007), the probability of

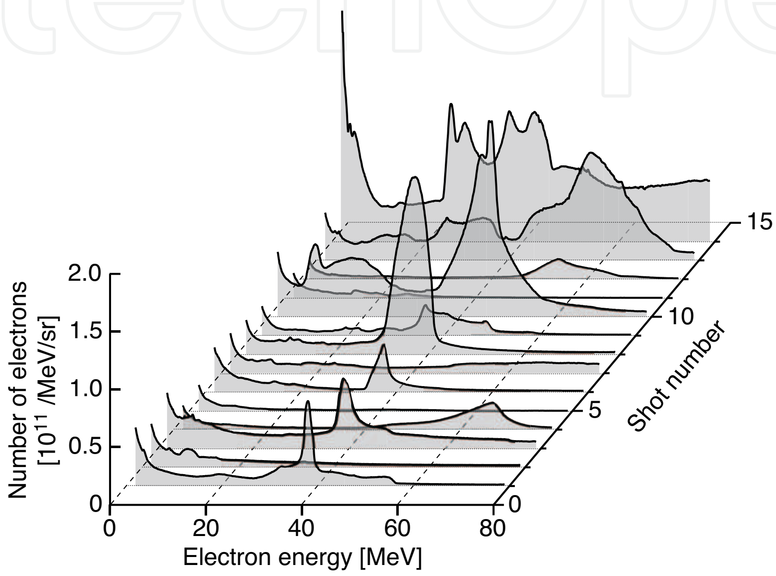

Fig. 4. Electron energy spectra obtained by sequential 14 shots under the same experimental conditions as those giving the result shown in Fig. 3. The probability of QME beam generation is 70%.

QME beam generation was a few tens of percent. The probability in the present experiment increased by a factor of 3, as compared with our previous experiment. It has been pointed out that there is a threshold energy of a laser pulse for stable generation of QME beams, which depends on the electron density of the plasma and the laser pulse duration (Mangles et al., 2007). Our present experimental conditions are in the range for stable generation predicted by scaling in Ref. (Mangles et al., 2007).

Figure 5 shows the distribution of the peak energy and the charge in the monoenergetic peak of QME beams for about 50 shots obtained under the same conditions as those giving the result shown in Fig. 3. A QME beam with a peak energy of up to 75 MeV was produced. A QME beam containing up to 88 pC in the peak at the energy of 48 MeV was also produced. In this case, the total energy of electrons in the peak was 4.2 mJ. This means that the efficiency of energy conversion from the laser pulse to the electron beam was 1%. Table 1 lists mean values and standard deviations of the parameters of QME beams obtained in about 50 shots shown in Fig. 5. The beam pointing means the angular deviation of the beam center from the laser propagation axis in the vertical direction. Although the probability of QME beam generation increases, shot-to-shot fluctuations in the charge and the energy spread are still large. The suppression of the fluctuations in the beam parameters is a key issue toward a next step.

Figure 6 shows the dependence of electron energy spectra on the electron density of the plasma, where the laser power is fixed at 8.3 TW. The electron density was varied by

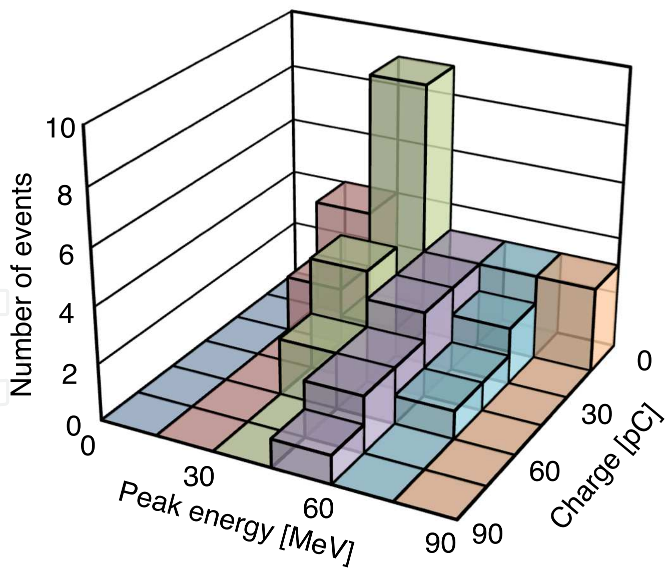

Fig. 5. Histogram showing the distribution of the peak energy and the charge in the monoenergetic peak of QME beams for about 50 shots obtained under the same conditions as those giving the result shown in Fig. 3.

Parameters	Mean $\pm$ Standard deviation
Peak energy	49 ± 15 MeV
Relative energy spread	22 ± 12 %
Charge in the monoenergetic peak	24 ± 20 pC
Divergence angle in the vertical direction (FWHM)	7.1 ± 4.0 mrad
Beam pointing in the vertical direction	± 7.8 mrad

Table 1. Statistics of the parameters of QME beams obtained in about 50 shots shown in Fig. 5.

controlling the gas jet density. As described above, QME beams were generated at an electron density of 1.6×10^{19} cm^{-3}, as shown by the solid curve. At a lower electron density of 1.3×10^{19} cm^{-3}, high-energy electrons were not observed, as shown by the dotted curve. On the other hand, at a higher density of 1.9×10^{19} cm^{-3}, the electron energy spectrum was a Maxwell-like distribution, and no clear monoenergetic peaks were seen, as shown by the dash-dotted curve. QME beams can be generated only in the narrow electron density region around 1.6×10^{19} cm^{-3}. This result shows that plasma density control is crucially important for the generation of QME beams.

3.3 Effect of a nanosecond prepulse on quasi-monoenergetic electron beam generation

There are many issues that must be controlled for stable generation of QME beams in laser-plasma interactions. Among them, the control of a prepulse and a preformed plasma is one key issue. In this subsection, we show the effects of a nanosecond prepulse on QME beam generation and propagation of an intense laser pulse.

The experimental conditions have been already shown in Sec. 3.1. The identical off-axis parabolic mirror and super sonic nozzle were used. As described in Sec. 3.1, the contrast ratios of femtosecond prepulses to a main pulse were kept to be less than 10^{-6}. The length of a nanosecond prepulse caused by amplified spontaneous emission (ASE) was controlled by varying the extraction time of the main pulse at the pulse cleaner.

Dependence of electron beam characteristics on length of nanosecond prepulse

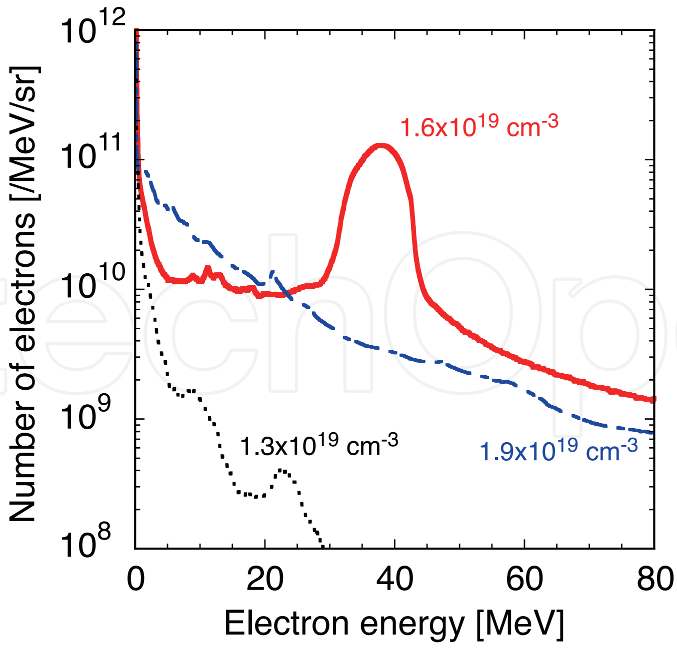

Fig. 6. The electron energy spectra observed for different electron densities of 1.3×10^{19} (dotted curve), 1.6×10^{19} (solid curve), and 1.9×10^{19} cm^{-3} (dash-dotted curve), respectively. To obtain QME beams, plasma density control is important.

Figure 7(a) shows a series of electron energy spectra obtained by 21 consecutive shots at a repetition rate of 1 Hz from a plasma with an electron density of 1.9×10^{19} cm^{-3} produced by an 8.5-TW laser pulse. The electron energy spectra were obtained by optimizing the extraction time of the main pulse at the pulse cleaner in addition to the optimization of the electron density. Here, this time is defined as the extraction time of the main pulse, $t_{\text{ext}} = 0$ ns. Figure 7(b) shows a series of electron energy spectra obtained by 17 consecutive shots at a repetition rate of 1 Hz for the different extraction time $t_{\text{ext}} = -2.5$ ns at the same laser power and electron density. The length of the nanosecond prepulse is longer, as the extraction time becomes earlier. As shown in Fig. 7(a), in most of shots, a monoenergetic peak was observed. In contrast, when the length of the nanosecond prepulse was long, monoenergetic peaks in the low energy range were observed only in a few shots among 17 consecutive shots as shown in Fig. 7(b). No monoenergetic peaks in the high energy range were observed. Furthermore,

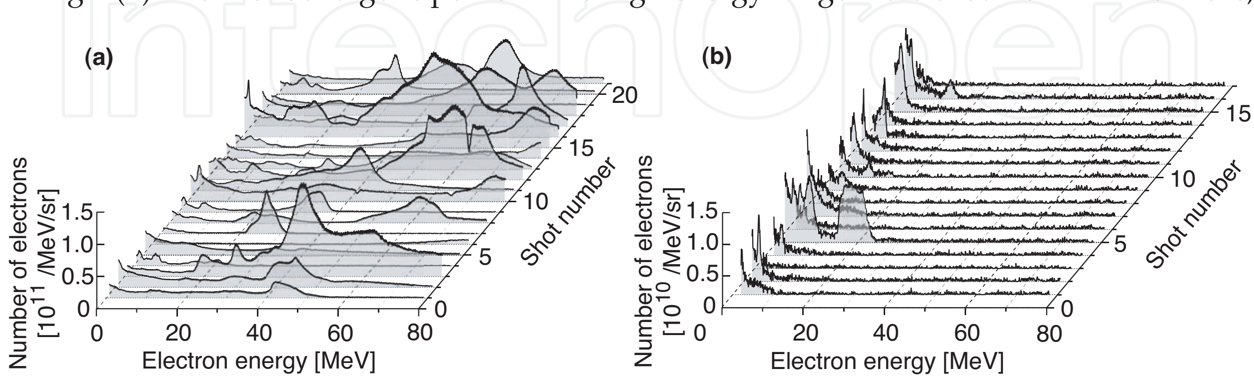

Fig. 7. Series of electron energy spectra obtained by about 20 consecutive shots at a repetition rate of 1 Hz for the different extraction times of the main pulse at the pulse cleaner: (a) $t_{\text{ext}} = 0$ ns and (b) $t_{\text{ext}} = -2.5$ ns.

the scale of the number of electrons in Fig. 7(b) is one-tenth of that in Fig. 7(a). The probability of the generation of QME beams was estimated according to the criteria described in Sec. 3.2. QME beams are obtained in 17 shots among 21 shots in the case of Fig. 7(a). The probability of QME beam generation is 81%, if the shot-to-shot fluctuations of the peak energy, the number of electrons, and so on are ignored. The probability of QME beam generation is 0 in the case of Fig. 7(b) according to the criteria described in Sec. 3.2.

Figure 8 shows the dependence of the probability of the QME beam generation (closed circles) and the laser energy (open triangles) on the extraction time of the main pulse at the pulse cleaner. Each data point of the probability was obtained with more than 10 consecutive shots at a repetition rate of 1 Hz. The electron density of the plasma was 1.9×10^{19} cm^{-3} for all data points. Notably, a few data points overlap at $t_{\rm ext} = -2.5$, -1.5, and $+1.5$ ns, when the probability is 0. The data points for the probability of QME beam generation are divided into three groups. When the length of the nanosecond prepulse is long ($t_{\rm ext} \sim -2$ ns), the probability is quite low. In contrast, when the nanosecond prepulse is suppressed ($t_{\rm ext} \sim 0$ ns), the probability dramatically increases and is close to 90%. This result shows that it is necessary to suppress a nanosecond prepulse for generation of QME beams. When the extraction time is too late ($t_{\rm ext} = +1.5$ ns), the probability becomes quite low again. This is due to the reduction in the laser energy as shown in Fig. 8.

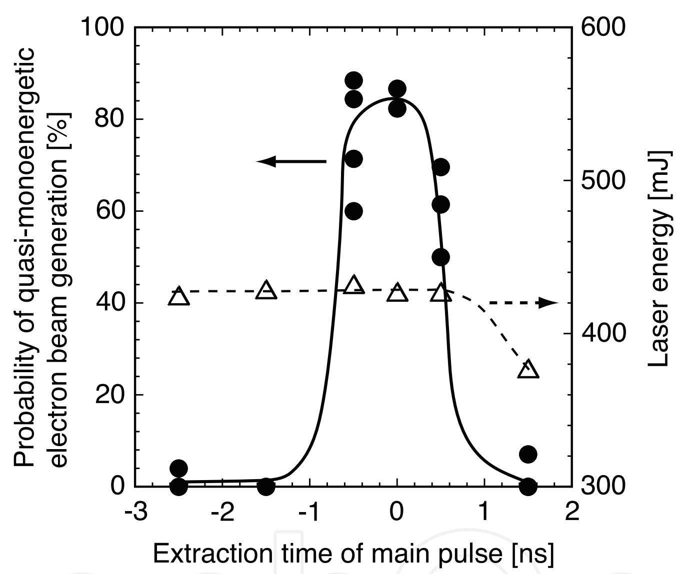

Fig. 8. Dependence of the probability of QME beam generation (closed circles) and the laser energy (open triangles) on the extraction time of the main pulse at the pulse cleaner. With the earlier extraction time, the length of a nanosecond prepulse is longer. For generation of QME beams, the suppression of the nanosecond prepulse is necessary.

The optimum electron density for QME beam generation in the experiment presented in this subsection was slightly higher than that of the results in shown in Sec. 3.2, although the experimental conditions were very close. The small difference of the laser conditions may cause the difference of the optimum electron density.

Plasma diagnostics

Figures 9(a) and (b) show a shadowgraph image and a horizontal profile of the image along the laser propagation axis for $t_{\rm ext} = -2.5$ ns, respectively. The laser pulse propagates from left to right in the image. The black area is the shadow of the nozzle and the nozzle exit position is shown by the white area. The image was taken at 1 ps before the arrival of the main pulse at the focal position. When the length of a nanosecond prepulse is long, a preformed plasma is observed around the vacuum focal position as denoted by arrows, although the image in Fig. 9(a) is not clear. As shown in Fig. 9(b), the length of the preformed plasma is approximately 200 μm, which is close to the Rayleigh length. Because the time delay of the probe pulse is -1 ps, the preformed plasma may be produced by a picosecond prepulse. In another experiment using an 8-TW laser pulse, formation of a preformed plasma was observed in a shadowgraph image taken at several tens of picoseconds before the arrival of the main pulse for $t_{\mathrm{ext}} = -2.5$ ns. Then, we think that the preformed plasma shown in Fig. 9 was produced by a nanosecond prepulse.

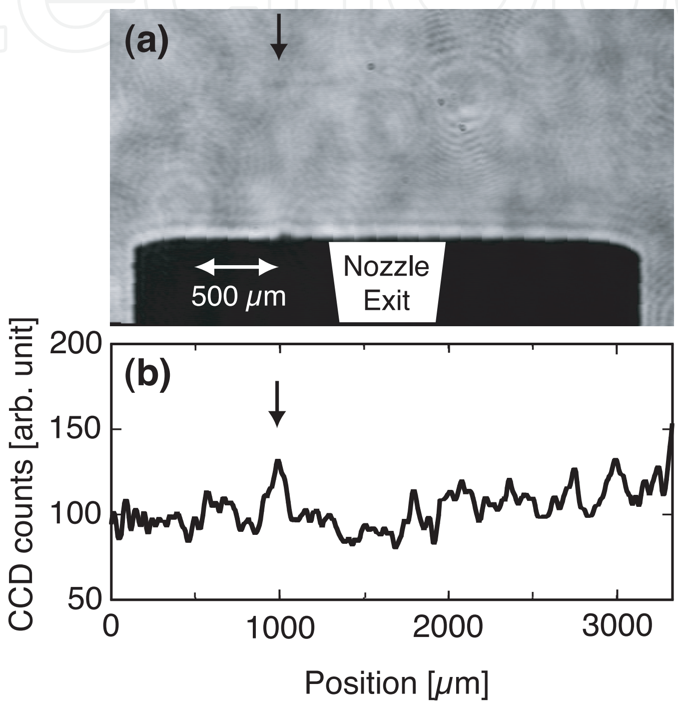

Fig. 9. (a) Typical shadowgraph image and (b) horizontal profile of the image along the laser propagation axis for the extraction time, $t_{\mathrm{ext}} = -2.5$ ns. The image is taken at 1 ps before the arrival of the main pulse at the focal position. A preformed plasma is observed as denoted by the arrows.

Figure 10 shows typical side-scattered light images observed for the different extraction times: (a) $t_{\mathrm{ext}} = 0$ ns and (b) $t_{\mathrm{ext}} = -2.5$ ns, respectively. The laser pulse propagates from left to right in the images. The dotted circle indicates the nozzle exit position. Both the images were observed through filters with the same attenuation and the laser energies were almost same shown in Fig. 8. When the nanosecond prepulse was suppressed (Fig. 10(a)), the image was similar to that suggesting the formation of a plasma channel reported in Refs. (Masuda et al., 2007; Miura et al., 2005). In contrast, when the length of the nanosecond prepulse was long, strong side-scattered light was observed as shown in Fig. 10(b). The image was quite different from that reported in Refs. (Masuda et al., 2007; Miura et al., 2005). The main pulse is strongly scattered, because the density profile of the preformed plasma is unsuitable for guiding the laser pulse. The remnant energy of the main pulse is insufficient to excite the plasma wave with a large amplitude. Then, no energetic electrons are accelerated. The side-scattered light image shown in Fig. 10(b) suggests that a certain fraction of the energy of the main pulse is scattered by the preformed plasma.

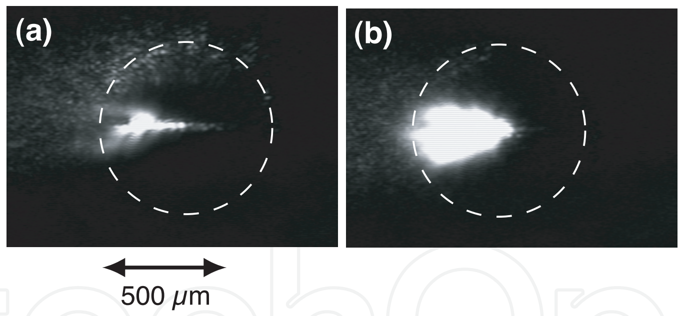

Fig. 10. Typical side-scattered light images observed for the different extraction times: (a) $t_{\text{ext}} = 0$ ns and (b) $t_{\text{ext}} = -2.5$ ns. The both images are observed through filters with the same attenuation. When the length of the nanosecond prepulse is long, the strong side-scattered light is observed.

3.4 Analysis on electron acceleration using two-dimensional particle-in-cell simulations

3.4.1 Analysis on quasi-monoenergetic electron beam generation

Conditions of two-dimensional particle-in-cell simulations

To investigate in detail the generation of QME beams shown in Sec. 3.2, we have developed a two-dimensional particle-in-cell (2D-PIC) simulation code using a moving window technique. The moving window had $127 \times 127 \mu\text{m}^2$ size with 2000×1000 cells containing 5 particles per cell. Simulations were conducted on the x-y plane. The laser propagation direction and the polarization direction were set in the x- and the y-axes. The laser pulse had a transverse profile with a TEM_{00} Hermite-Gaussian mode and a cosine temporal envelope. The laser pulse energy, the spot size, and the pulse duration were 400 mJ, 9 μm at the FWHM and 50 fs at the FWHM, respectively. The electron density profile along the x-axis was set to be similar to the measured density profile of a gas jet. The center of the gas jet in the experiment was set at $x = 0$. The initial electron density raised at $x = -960$ μm, and smoothly increased to the maximum of 1.6×10^{19} cm^{-3} at $x = -350$ μm. To investigate the interaction for a long propagation length, it was assumed that the electron density was constant from the position where the density reached the maximum value. The focal position in vacuum was set at $x = -300$ μm. The density profile was uniform along the y-axis.

Simulation results

Figure 11 shows snapshots of the electron distribution on the x-y plane (a)-(c) and the number of electrons as functions of the energy and the angle of the momentum vector (d)-(f) for three different positions. In Figs. 11(a)-(c), the leading edge of the laser pulse is near the right edge and each electron is colored by its energy. At $x = 170$ μm, electrons are not trapped in a plasma wave, because the amplitude of the plasma wave is small. The high-energy electrons are not observed in Fig. 11(d). After some time, trapping of electrons occurs due to sufficient growth of the plasma wave, and a monoenergetic electron bunch is trapped and accelerated in the first period of the plasma wave at $x = 570$ μm, as seen in Figs. 11(b) and (e). The fine structure in the monoenergetic bunch seen in Fig. 11(b) is due to the interaction of electrons with the laser field. At $x = 1050$ μm, the trapped electrons enter the deceleration phase and dissipate the energy. Then, the monoenergetic component disappears, as seen in Fig. 11(f). This result shows that the extraction position of electrons from the plasma is important for QME beam generation. The predicted optimum laser propagation length from the focal position is 870 μm, which is close to the gas jet length of approximately 1 mm in the experiment. This suggests that the generation of a QME beam is brought about by matching the laser propagation length with the gas jet length.

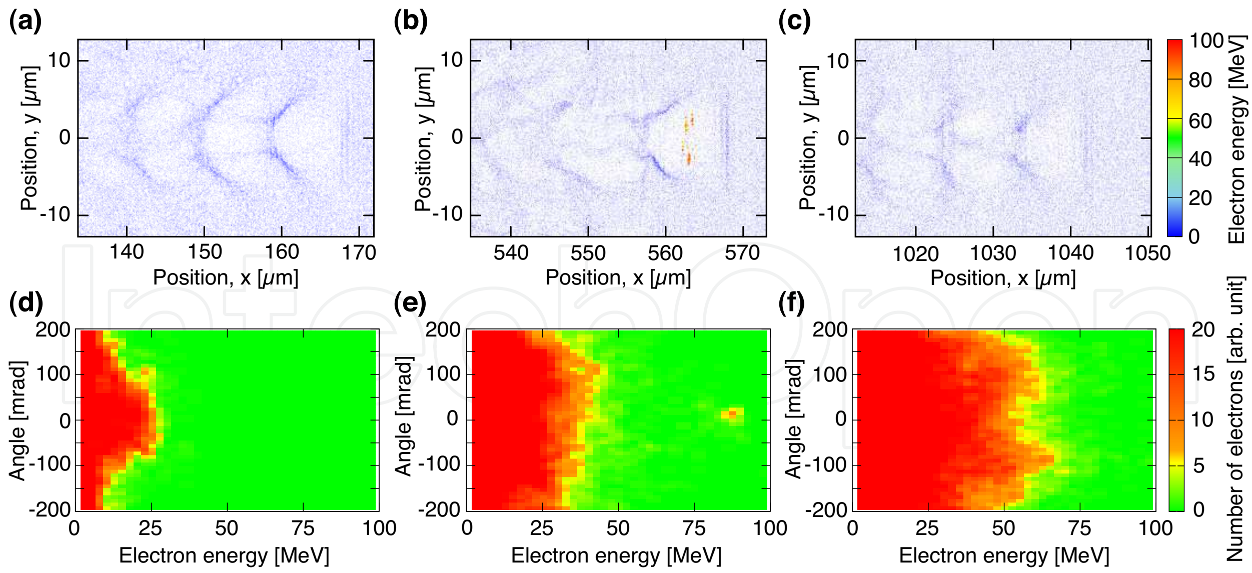

Fig. 11. 2D-PIC simulation results for an electron density of 1.6×10^{19} cm^{-3}. Snapshots of the electron distribution on the x-y plane (a)-(c) and the number of electrons as functions of the energy and the angle of the momentum vector (d)-(f) are shown for three different positions.

The generation of a monoenergetic bunch with a peak energy of 90 MeV, a relative energy spread of 6% at the FWHM, and a divergence angle of 28 mrad at the FWHM is predicted. The predicted values of the monoenergetic component are fairly close to the experimental results. As seen in Fig. 11(e), only the monoenergetic component has a small divergence angle. In contrast, the low-energy component has a large divergence. The simulation result explains the difference in the beam divergence between the monoenergetic and the low-energy components, as seen in Fig. 3(a).

Simulations were conducted for electron densities of 1.3 and 1.9×10^{19} cm^{-3}. For all the densities, including 1.6×10^{19} cm^{-3}, electron injection occurs and a monoenergetic electron bunch is formed in the first period of the plasma wave, immediately after the amplitude of the plasma wave reaches the maximum. However, the growth rate of the plasma wave depends on the electron density, and the laser propagation lengths required for electron injection are different for each electron density. The growth rate is larger as the electron density is higher. At an electron density of 1.3×10^{19} cm^{-3}, the laser propagation length required for electron injection is longer than the gas jet length of 1 mm in the experiment. Because the electron injection does not occur inside the gas jet, high-energy electrons are not observed. In contrast, at an electron density of 1.9×10^{19} cm^{-3}, the electron injection occurs too early, and the trapped electrons enter the deceleration phase, so the energy dissipates at the end of the gas jet. Then, a monoenergetic peak is not observed. The simulation results also explain the density dependence of the electron energy spectra shown in Fig. 6 (Masuda & Miura, 2009).

3.4.2 Analysis on effect of a nanosecond prepulse on quasi-monoenergetic electron beam generation

Preformed plasma model in simulation

To investigate effects of a nanosecond prepulse on QME beam generation shown in Sec. 3.3, 2D-PIC simulations were also conducted. The dynamics both of a preformed plasma produced by a nanosecond prepulse and the propagation of a femtosecond laser pulse in a millimeter-scale plasma can not be treated simultaneously in the PIC simulation, because their time scales are significantly different. In the present simulation, the preformed plasma is formed by giving a density modification of the initial electron and ion distributions.

It is assumed that a preformed plasma with a transversely hollow density profile is formed due to the expansion during a few nanoseconds. Singly ionized helium ions are distributed inside a preformed plasma region, and neutral helium atoms are distributed in the calculation region except for the preformed plasma region. The initial electron density is zero in the entire calculation region. The PIC simulation code includes the optical field ionization process. The leading edge of a laser pulse ionizes neutral atoms and singly ionized ions up to doubly ionized state. The electron density inside the preformed plasma region, where singly ionized helium ions are initially distributed, is half of that in the region, where neutral helium atoms are initially distributed. As a result, a preformed plasma with a transversely hollow density profile is formed. The main body of a laser pulse propagates in the preformed plasma. The details in a model to create a preformed plasma with a hollow density profile in the calculation have been described in Ref. (Masuda & Miura, 2010).

It is found that the longitudinal size of the preformed plasma is approximately 200 μm from the shadowgraph image as shown in Fig. 9(b). Then, the longitudinal size of the preformed plasma region is assumed to be 230 μm, corresponding to the Rayleigh length. Although the observed transverse size of the preformed plasma is limited by the spatial resolution, the transverse size is assumed to be 9 μm, corresponding to the laser spot diameter. The preformed plasma region is set at the vacuum focal position of the laser pulse, because the preformed plasma is observed around the vacuum focal position as shown in Fig. 9(a). Except for the preformed plasma conditions, simulation conditions are the same as those shown in Sec. 3.4.1. The case above described is referred as preformed plasma case. In no preformed plasma case, neutral helium atoms are initially distributed in the entire calculation region and the initial electron density is zero.

Simulation results

Figures 12(a) and (b) show spatial evolutions of transverse envelopes of the laser electric field represented by the normalized vector potential on the x-y plane in no preformed plasma case and preformed plasma case. The spatial evolutions are obtained from the transverse envelopes of the peak amplitude of the laser electric field for every 255 time steps. In no preformed plasma case, the laser pulse focused at $x = -300$ μm propagates by forming a narrow channel over the Rayleigh length due to the relativistic self-focusing effect. A part of the laser energy is scattered away from the channel. In preformed plasma case, the scattering of the laser pulse increases as shown in Fig. 12(b). This result explains the experimental observation of the strong side-scattered light image shown in Fig. 10(b). Due to the increase in the laser scattering, the peak intensity of the laser pulse in the channel decreases in preformed plasma case.

Figures 13(a) and (b) show the electron energy spectra as a function of the position of the laser pulse in no preformed plasma case and preformed plasma case. The spatial evolutions are obtained from the electron energy spectra calculated for the electrons with the angle of the momentum vector with respect to the laser propagation direction in the range of ± 50 mrad in the moving window for every 255 time steps. In no preformed plasma case, a clear monoenergetic peak is formed at $x \sim 600$ μm and the maximum peak energy reaches ~ 80 MeV as shown in Fig. 13(a). This position ($x \sim 600$ μm), which is the optimum extraction position of a monoenergetic electron bunch, is close to the end of the gas jet in the experiment. In no preformed plasma case, a QME beam is produced, because matching the length of the laser propagation with the gas jet length is achieved. This result is quite similar to that shown in Sec. 3.4.1.

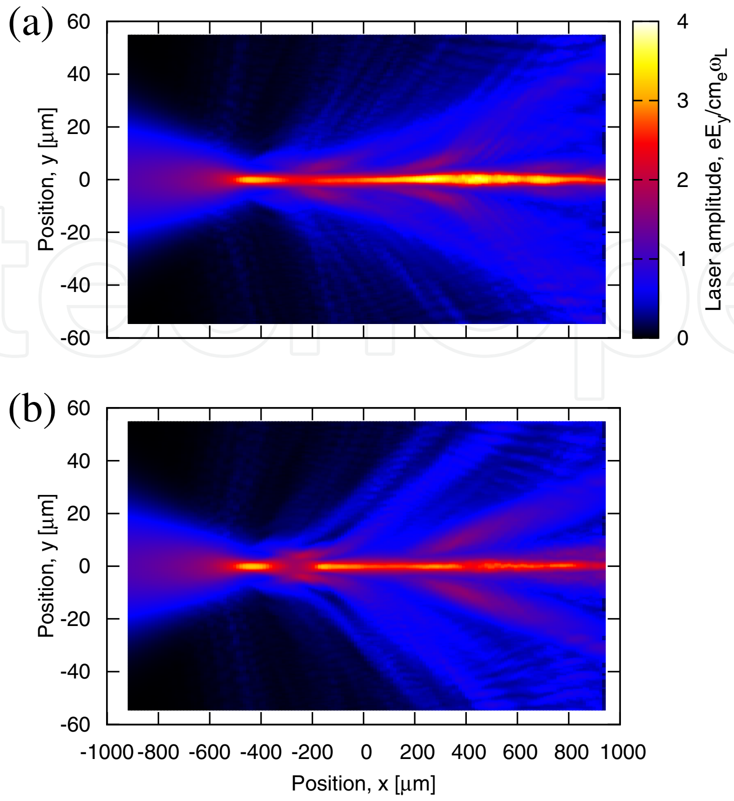

Fig. 12. Spatial evolution of transverse envelopes of the laser electric field on the x-y plane in (a) no preformed plasma case and (b) preformed plasma case. Scattering of the laser pulse increases and the laser intensity on the propagation axis decreases in preformed plasma case.

In contrast, in preformed plasma case, the growth rate of the plasma wave is smaller than that in no preformed plasma case due to the low peak amplitude of the laser field as shown in Fig. 12(b). The time, when the amplitude of the plasma wave reaches the maximum and the electron injection occurs, is delayed and the required laser propagation length becomes longer than that in no preformed plasma case. A monoenergetic peak is formed at $x \sim 700\,\mu$m as shown in Fig. 13(b). However, the monoenergetic peak is not clear, because the amount of injected electrons is small. The optimum extraction position of a monoenergetic electron bunch ($x \sim 700\ \mu$m) is outside the gas jet region in the experiment. This means that the acceleration length is extremely short in the experiment. In preformed plasma case, a QME beam is not obtained, because the required condition, that is matching the laser propagation length with the gas jet length, is not satisfied due to the low growth rate of the plasma wave. The simulation results using a simple model for a preformed plasma qualitatively explain the experimental results of effects of a nanosecond prepulse on QME beam generation.

4. X-ray generation by laser Compton scattering using laser-accelerated quasi-monoenergetic electron beam

4.1 Ultrashort X-ray source based on laser Compton scattering

An ultrashort electron pulse with a duration of the order of a few tens of femtoseconds can be obtained in LPA. In addition, there is the potential for realizing compact electron accelerators.

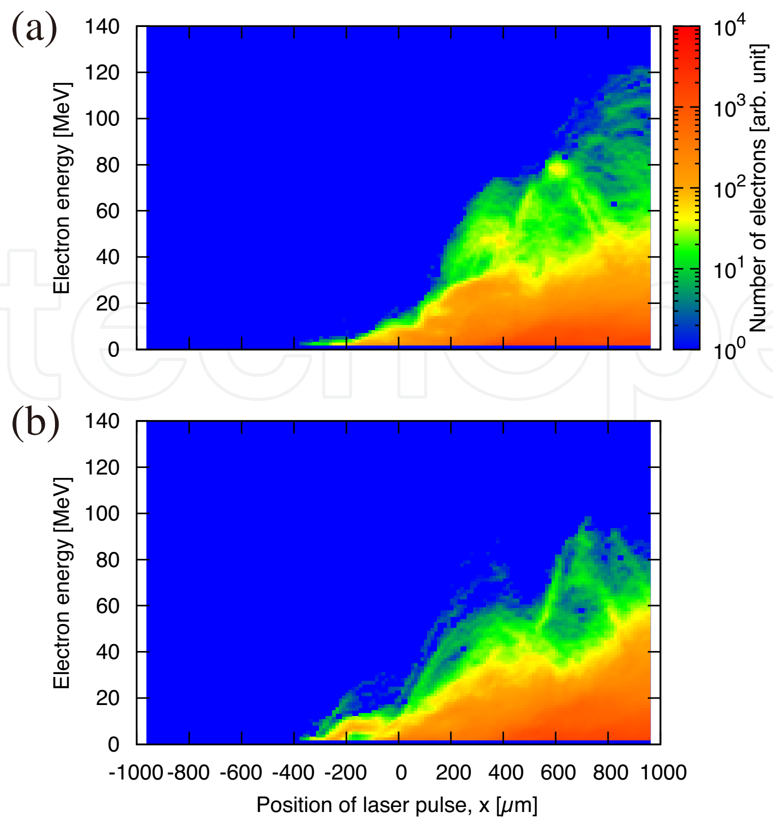

Fig. 13. Electron energy spectra as a function of the position of the laser pulse in (a) no preformed plasma case and (b) preformed plasma case. In no preformed plasma case, a clear monoenergetic peak with an energy of 80 MeV is formed at the position, $x \sim 600\,\mu$m, which corresponds to the end of the gas jet in the experiment. At the same position, a clear monoenergetic peak is not observed in preformed plasma case.

The set of such unique characteristics enables us to realize compact, all-optical, ultrashort radiation sources in the wavelength range from extreme ultraviolet to X-ray. One of them is an X-ray source based on laser Compton scattering, that is scattering of photons by energetic electrons. Laser Compton scattering X-ray sources have attracted much attention for their potential of applications to medical imaging (Ikeura-Sekiguchi et al., 2008), because they produce a well-collimated, quasi-monochromatic X-ray beam, the photon energy of which is tunable, in a small facility, as compared with synchrotron radiation sources.
So far, generation of a femtosecond X-ray pulse by laser Compton scattering has been demonstrated by using a femtosecond laser pulse and a picosecond electron pulse from rf accelerators (Schoenlein et al., 1996; Yorozu et al., 2002). The X-ray pulse duration is determined by the interaction time between the laser and electron pulses. To obtain a femtosecond X-ray pulse, 90° scattering geometry should be adopted for a picosecond electron pulse. In contrast, 180° scattering (head-on collision) geometry can be adopted for a femtosecond electron pulse obtained by LPA. There are some advantages of using 180° scattering geometry. The photon energy of X-rays is higher than that for 90° scattering geometry, even though the electron energy and the wavelength of a laser pulse are the same. In addition, the X-ray yield is higher than that for 90° scattering geometry, even though the charge of an electron beam and the energy of a laser pulse are the same. Generation of X-rays with energies around 1 keV by laser Compton scattering has been demonstrated using

a laser-accelerated electron beam with a Maxwell-like energy distribution. (Schwoerer et al., 2006). In this section, X-ray generation by laser Compton scattering using a laser-accelerated quasi-monoenergetic electron beam is described.

4.2 Experimental conditions

Figure 14 shows the experimental setup. Laser pulses for electron acceleration and laser Compton scattering are referred as main laser pulse and colliding laser pulse. A p-polarized main laser pulse (700 mJ, 40 fs, 800 nm) was focused onto the edge of a helium gas jet using an $f/14$ off-axis parabolic mirror with a focal length of 720 mm. The laser spot diameter in vacuum was 13 μm at the FWHM. The energy concentration within the e^{-2} spot was 50% of the total laser energy. The peak intensity was 4.7×10^{18} W/cm^2, corresponding to the normalized vector potential of 1.4. The gas jet was ejected from a supersonic nozzle with a conical shape. The diameter of the nozzle exit was 1.6 mm and the Mach number was 5. The focal position was set at 1 mm above the nozzle exit.

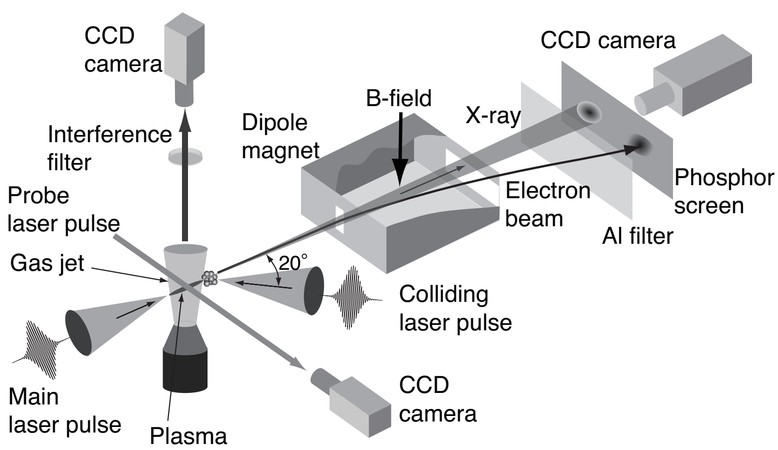

Fig. 14. Experimental setup for X-ray generation by laser Compton scattering using laser-accelerated electron beam.

A p-polarized colliding laser pulse (140 mJ, 100 fs, 800 nm) was focused around the exit of the main laser pulse from the gas jet using an $f/6$ off-axis parabolic mirror with a focal length of 300 mm. The laser spot diameter in vacuum was 9 μm at the FWHM. The incident angle of the colliding laser pulse was 20° to the propagation axis of the main laser pulse. X-rays produced by laser Compton scattering were emitted on the coaxial direction of an electron beam. The electron beam was bended by a magnetic field and spatially separated from the X-rays. Both X-rays and electrons were simultaneously incident on a $Gd_2O_2S:Tb$ phosphor screen (DRZ-HGH) through a 115-μm-thick Al filter. The images of X-rays and energy-resolved electrons were observed with a CCD camera. Electrons with an energy higher than 35 MeV were detected. The charge can be estimated, because the sensitivity of the detection system was calibrated for electrons (Masuda et al., 2008). The photon energy range of detected X-rays was higher than 10 keV from the calculated sensitivity of the phosphor screen.

For synchronized collision of a colliding laser pulse with a laser-accelerated electron beam, a time-resolved shadowgraph image along the propagation axis of the main laser pulse was observed using a 60-fs probe laser pulse. A side-scattered light image through an interference filter of 800 nm, that is Thomson-scattered light image, was also observed from the top of the gas jet.

The conditions for electron acceleration were different from those shown in Sec. 3.2. In prior, we confirmed that QME beams with a peak energy from 50 to 100 MeV and a charge in the monoenergetic peak of several tens of picocoulombs were obtained from a plasma with an electron density of 1.7×10^{19} cm^{-3} (Miura et al., 2011).

4.3 Synchronized collision of femtosecond laser pulse with electron beam

For X-ray generation by laser Compton scattering, synchronized collision of a colliding laser pulse with a laser-accelerated electron beam is required. A laser-accelerated electron beam is emitted in the coaxial direction of a main laser pulse and temporally close to a main laser pulse. Then, achieving the synchronized collision of the colliding laser pulse with the laser-accelerated electron beam is equivalent to achieving the synchronized collision of the main and colliding laser pulses. Figures 15(a)-(c) show typical shadowgraph images observed for different delay times of the probe laser pulse to the main laser pulse: (a) -1.33 ps, (b) -0.67 ps, and (c) 0 ps, respectively. The main laser pulse propagated from right to left, and the

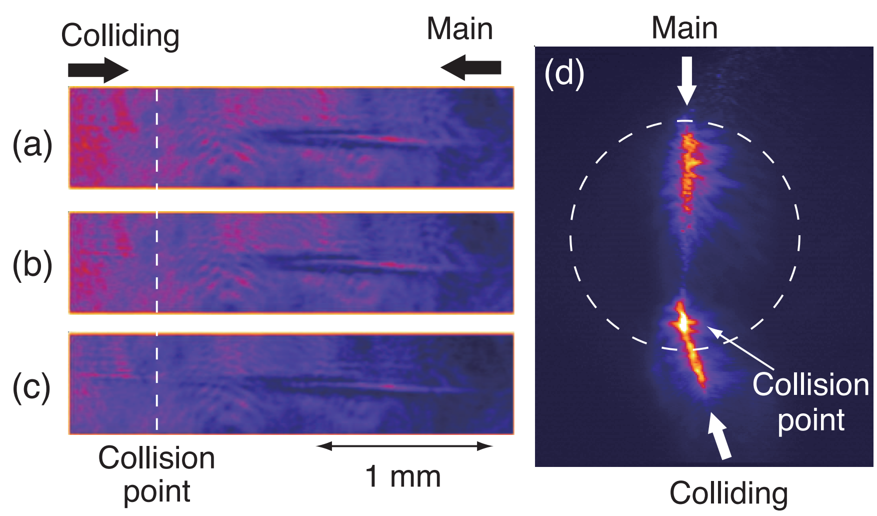

Fig. 15. (a)-(c) Shadowgraph images observed for different delay times of a probe laser pulse to a main laser pulse: (a) -1.33 ps, (b) -0.67 ps, and (c) 0 ps. (d) Thomson-scattered light image when the synchronized collision of the main and colliding laser pulses is achieved. The bright spot indicates the collision point of the two laser pulses.

colliding laser pulse propagated from left to right. The ionization fronts of the two laser pulses approached each other with varying the delay of the probe laser pulse. As seen in Fig. 15(c), the ionization fronts of the two laser pulses overlapped, and two laser pulses collided. The optical path length and the focal position in the vertical direction of the colliding laser pulse were adjusted using the shadowgraph images.

The collision point on the horizontal plane was set using a Thomson-scattered light image observed from the top of the gas jet as shown in Fig. 15(d). The dotted circle shows the position of the nozzle exit with 1.6-mm diameter. In Fig. 15(d), the main laser pulse propagated from top to bottom and the colliding laser pulse propagated from lower right to upper left in the direction of 20° to the main laser propagation axis. As shown by the thin arrow, a bright spot was observed, only the synchronized collision of the two laser pulses was achieved. It is supposed that the bright spot indicates the collision point of the two laser pulses. The collision point was set at the edge of the nozzle exit, which was near the extraction position of an electron beam from a plasma.

4.4 X-ray generation

X-rays produced by laser Compton scattering were observed, when a QME beam with a considerably high charge was obtained. Figure 16(a) shows an image of X-rays. The image was obtained with a single shot. From the energy-resolved electron image simultaneously observed with the image shown in Fig. 16(a), the peak energy and the charge in the monoenergetic peak of the QME beam were estimated to be 50 MeV and 30 pC, respectively. Figure 16(b) shows the intensity profile of the image in the vertical direction. The divergence angle in vertical direction was 5 mrad at the FWHM. The divergence angle in horizontal direction was 7 mrad at the FWHM. In laser Compton scattering, a collimated X-ray beam can be obtained. The divergence angle of the X-ray beam is given by $\sim 1/\gamma$. Here, γ is the Lorentz factor of an electron energy. The divergence of an X-ray beam is estimated to be approximately 10 mrad from the observed peak energy of 50 MeV. The observed divergence angle was close to the predicted value from the electron energy. The maximum photon energy

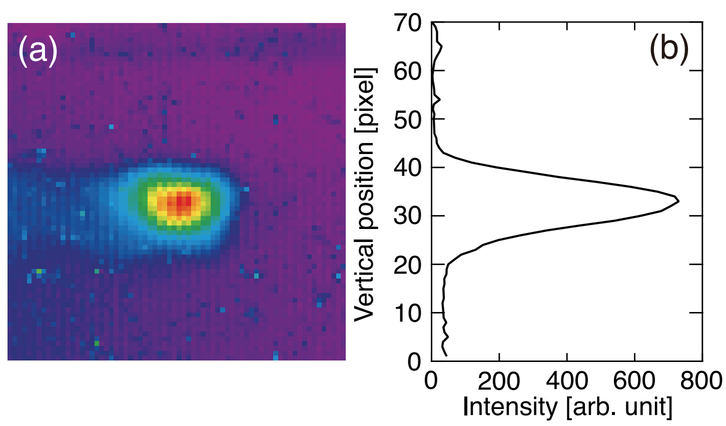

Fig. 16. (a) Image of X-rays produced by laser Compton scattering and (b) the vertical profile of the image. A well-collimated X-ray beam with a divergence angle of 5 mrad at the FWHM in the vertical direction is observed.

of the X-rays was estimated to be 60 keV from the peak energy of the QME beam and the interaction angle between the electron and laser pulses. The X-ray yield was also estimated to be approximately 10^5 photons/pulse from the charge of the QME beam and the irradiation conditions of the colliding laser pulse by including the dependence of the differential cross section of scattering on the scattered angle of X-rays.
The allowance range of the delay between the main and colliding laser pulses for X-ray generation was investigated. The allowance range was approximately 100 fs, which was close to the duration of the colliding laser pulse. This result suggests that a pulse duration of a QME beam is nearly equal to or less than 100 fs. The generation of an ultrashort electron pulse has been demonstrated at the same time.

5. Recent progress toward next step

The present status of LPA research has been presented as an example of works conducted at the AIST. In addition to our works, various works on improvement of the performance of electron beams have been so far conducted, and characterization and applications of electron beams have been also demonstrated. In this section, these woks are briefly reviewed.

5.1 Toward more energetic electron acceleration

LPA is expected as technologies obtaining extremely high energy particles using the extremely high accelerating field. A longer plasma and a longer acceleration length are required for obtaining more energetic electrons. One of the approaches is to form a plasma waveguide for guiding an intense laser pulse using a preformed plasma produced by a discharge, which has a transversely hollow density profile. A 1-GeV QME beam has been produced from a 3-cm-long capillary discharge plasma (Leemans et al., 2006). After that, several groups have reported the generation of GeV-class QME beams from a centimeter-scale capillary discharge plasma (Kameshima et al., 2008; Karsch et al., 2007; Rowlands-Rees et al., 2008). On the other hand, GeV-class electron beams have been also produced using a centimeter-scale gas jet based on a self-guiding of an intense laser pulse (Clayton et al., 2010; Hafz et al., 2008).

Experiments to accelerate extremely high energy electrons have been also conducted using a PW-class laser system of single shot operation. Energetic electron beams have been produced from a hollow glass capillary attached with a gold cone irradiated by an intense laser pulse (Kitagawa et al., 2004; Mori, Sentoku, Kondo, Tsuji, Nakanii, Fukumochi, Kashihara, Kimura, Takeda, Tanaka, Norimatsu, Tanimoto, Nakamura, Tampo, Kodama, Miura, Mima & Kitagawa, 2009). In this experiment, the gold cone attached at the entrance of a laser pulse plays an important role for the electron injection into a plasma wave driven inside the hollow capillary. Energetic electrons have been produced by the interaction of an intense laser pulse with a plasma preformed from a hollow plastic cylinder via laser-driven implosion (Nakanii et al., 2008). Electrons with energies of more than 600 MeV are observed from a 3-mm-long plasma tube.

5.2 Improvement, stabilization, and control of electron beam quality

Optical injection scheme

In a self-injection scheme, the injection of electrons into a plasma wave is based on the wave-breaking. The wave-breaking is a nonlinear phenomenon which is substantially unstable, and it is difficult to actively control it. Characteristics of electron beams are strongly affected by the shot-to-shot fluctuations of conditions of a gas jet, a laser pulse, and so on. Stabilization of electron beam qualities will be achieved by controlling the injection of electrons into a plasma wave. It is possible to control the injection of electrons into a plasma wave using multiple laser pulses. One laser pulse drives a plasma wave with an amplitude, in which wave-breaking does not occur, and other laser pulses control the injection of electrons into a plasma wave. This scheme is called optical injection scheme, or colliding pulse scheme. Although there have been several theoretical proposals (Esarey et al., 1997; Kotaki et al., 2004; Umstadter, Kim & Dodd, 1996), it took time for the experimental demonstration due to the requirement for using multiple laser pulses. Recently, experimental demonstrations of an optical injection scheme have been reported (Faure et al., 2006; Kotaki et al., 2009). When two counter-propagating laser pulses collide, a beat wave is formed and preaccelerates electrons in a plasma. The preaccelerated electrons are trapped into a plasma wave and accelerated. The stability of QME beam qualities has been improved, as compared with a self-injection scheme.

Plasma control in self-injection scheme

In a self-injection scheme, stabilization and improvement of electron beam qualities have been achieved by controlling the characteristics of a plasma.

In most experiments using a gas jet, a helium gas jet has been used. The pointing stability and divergence of QME beams have been improved by using an argon gas jet (Mori, Kondo, Mizuta, Kando, Kotaki, Nishiuchi, Kado, Pirozhkov, Ogura, Sugiyama, Bulanov, Tanaka, Nishimura & Daido, 2009). For an argon gas jet, a preformed plasma suitable for guiding a main pulse is produced by ASE accompanying a main pulse due to the lower ionization potential of argon than that of helium.

The increase in a charge and the decrease in a beam divergence have been achieved using a gas jet composed helium and controlled amounts of various high-Z gases (McGuffey et al., 2010; Pak et al., 2010). Optical field ionization of inner shell electrons of the high-Z gas plays an important role in increasing the number of electrons injected into a plasma wave. This is referred as ionization induced trapping.

As described in Sec. 5.1, a capillary discharge plasma has been used for producing a long plasma and guiding an intense laser pulse. With a steady-state-flow gas cell using a hollow capillary without discharge, stable generation of QME beams has been achieved (Osterhoff et al., 2008). The steady-state gas flow forms a reproducible, homogeneous gas distribution along the laser propagation direction, which brings about the stable QME beam generation.

An increase in a charge and a decrease in a divergence of electron beams have been observed by applying a static external magnetic field along the laser pulse propagation axis, although the electron energy spectra are Maxwell-like distributions (Hosokai et al., 2006). The shape of a preformed plasma suitable for guiding a main pulse is formed by applying a static magnetic field.

5.3 Demonstration of femtosecond electron pulse generation

A femtosecond electron pulse can be produced in LPA. To prove the generation of a femtosecond electron pulse, a temporal characterization of an electron pulse has been conducted. In the temporal characterization, coherent transition radiation (CTR) emitted at the plasma-vacuum boundary or through a thin metallic foil is used. An electron pulse duration is measured with an electro-optical sampling technique using CTR in the THz region, and the temporal resolution of several tens of femtoseconds has been achieved. (Debus et al., 2010; van Tilborg et al., 2006) An electron pulse duration is also estimated from the spectrum of CTR (Glinec et al., 2007; Ohkubo et al., 2007). Recently, generation of a few femtosecond electron pulse has been demonstrated using an optical injection scheme (Lundh et al., 2011).

Such ultrashort electron pulse is a useful tool to investigate physical and chemical kinetics of ultrafast phenomena initiated by ionization radiation referred as pulsed radiolysis. Applications of a laser-accelerated electron beam to pulsed radiolysis have been demonstrated (Brozek-Pluska et al., 2005).

5.4 Ultrashort X-ray radiation

Using a femtosecond electron pulse obtained in LPA, ultrashort short-wavelength radiation sources from extreme ultraviolet to X-ray can be obtained as the secondary source. Such ultrashort short-wavelength sources are attractive for applications to observe ultrafast phenomena such as time-resolved X-ray diffraction. As shown in Sec. 4, X-ray generation by laser Compton scattering using a laser-accelerated electron beam has been demonstrated (Miura et al., 2011; Schwoerer et al., 2006).

The generation of synchrotron radiation has been demonstrated by using a laser-accelerated QME beam through an undulator (Fuchs et al., 2009; Schlenvoigt et al., 2008). The wavelength of the radiation still remains visible to extreme ultraviolet due to the low electron energy. In the near future, the wavelength range will be extended to X-rays, as the electron energy increases.

Generation of keV X-rays by betatron radiation in a plasma has been demonstrated (Rousse et al., 2004). Laser-accelerated electrons undergo a transverse electric field in an ion channel, which is formed inside a low electron density region of a plasma wave. They undergo betatron oscillation and emitted a collimated X-ray beam. Generation of a short X-ray pulse of less than 1 ps has been proven by measuring the temporal variation of X-ray reflectivity of a crystal pumped by a femtosecond laser pulse (Phuoc et al., 2007).

Extreme ultraviolet radiations have been demonstrated by the laser light reflection from a plasma wave driven by an intense laser pulse (Kando et al., 2007; 2009). The plasma wave moving almost at the speed of light acts as a relativistic flying mirror, and brings about frequency upshift and compression of the incident laser pulse due to the double Doppler effect. This regime is one of notable methods for generation of ultrashort short-wavelength radiations using an intense laser pulse, although laser-accelerated electron beams are not used.

6. Summary and future prospects

In this chapter, we provide the overview of the present status of research on LPA. Remarkable progress such as QME beam generation has been made especially in the last several years. Although the quality and stabilization of electron beams have been improved, there is still room for improvement of beam qualities for practical applications. For further improvement of electron beam qualities, theoretical and experimental studies should be continued to answer various questions in physics of laser-plasma interactions and to explore new acceleration regime.

Compactness of a plasma accelerating electrons, corresponding to an electron gun and a series of rf cavities in rf accelerators, has been proven. However, an ultrashort ultraintense laser system for producing the plasma is still large, although the laser system is called "table-top" system. More compact laser system is necessary. In addition, the repetition rate of present laser systems is still 10 Hz. For increasing the average flux and luminosity, the development of an efficient laser system with much higher repetition rate is also dispensable. It is essential to conduct the research on plasma physics and the development of laser technologies in parallel.

There are several prominent features in LPA such as femtosecond electron pulse generation. It is important to prove promising applications that make the best use of the features of LPA. Several promising applications have been already demonstrated. It becomes a stage when the design of laser electron accelerators for practical applications should be conducted by including a laser system. The recent progress of ultrashort ultraintense laser technologies is rapid and remarkable. In addition, the recent progress of high performance computer system is also rapid and remarkable. It will play a major role to investigate physics in laser-plasma interactions by numerical simulations. The set of rapid progress of laser technologies and investigation of physics will dramatically improve the performance of laser-accelerated electron beams. In the near future, laser electron accelerators useful for fundamental physics, and industrial and societal applications will be realized.

7. Acknowledgments

I thank all the coworkers for their supports and fruitful discussion, especially S. Masuda, S. Ishii, K. Tanaka, T. Ooyama, R. Kuroda, and H. Toyokawa, who have contributed to the works presented here. A part of our works presented here was financially supported by the Budget for Nuclear Research of the Ministry of Education, Culture, Sports, Science and Technology (MEXT), Japan, based on the screening and counseling by the Atomic Energy Commission, the Advanced Compact Accelerator Development of the MEXT, and the Matsuo Foundation. I also wish to acknowledge the support of the Advanced Compact Accelerator Development Office of the National Institute of Radiological Sciences, Japan.

8. References

Amiranoff, F., Bernard, D., Cros, B., Jacquet, F., Matthieussent, G., Miné, P., Mora, P., Morillo, J., Moulin, F., Specka, A. E. & Stenz, C. (1995). Electron acceleration in Nd-laser plasma beat-wave experiments, *Phys. Rev. Lett.* 74: 5220–5223.

Aoyama, M., Yamakawa, K., Akahane, Y., Ma, J., Inoue, N., Ueda, H. & Kiriyama, H. (2003). 0.85-PW, 33-fs Ti:sapphire laser, *Opt. Lett.* 28: 1594–1596.

Brozek-Pluska, B., Gliger, D., Hallou, A., Malka, V. & Gauduel, Y. A. (2005). Direct observation of elementary radical events: low- and high-energy radiation femtochemistry in solutions, *Rad. Phys. Chem.* 72: 149 – 157.

Bulanov, S. V., Pegoraro, F., Pukhov, A. M. & Sakharov, A. S. (1997). Transverse-wake wave breaking, *Phys. Rev. Lett.* 78: 4205–4208.

Cheriaux, G., Rousseau, P., Salin, F., Chambaret, J. P., Walker, B. & Dimauro, L. F. (1996). Aberration-free stretcher design for ultrashort-pulse amplification, *Opt. Lett.* 21: 414–416.

Clayton, C. E., Marsh, K. A., Dyson, A., Everett, M., Lal, A., Leemans, W. P., Williams, R. & Joshi, C. (1993). Ultrahigh-gradient acceleration of injected electrons by laser-excited relativistic electron plasma waves, *Phys. Rev. Lett.* 70: 37–40.

Clayton, C. E., Ralph, J. E., Albert, F., Fonseca, R. A., Glenzer, S. H., Joshi, C., Lu, W., Marsh, K. A., Martins, S. F., Mori, W. B., Pak, A., Tsung, F. S., Pollock, B. B., Ross, J. S., Silva, L. O. & Froula, D. H. (2010). Self-guided laser wakefield acceleration beyond 1 GeV using ionization-induced injection, *Phys. Rev. Lett.* 105: 105003.

Debus, A. D., Bussmann, M., Schramm, U., Sauerbrey, R., Murphy, C. D., Major, Z., Hörlein, R., Veisz, L., Schmid, K., Schreiber, J., Witte, K., Jamison, S. P., Gallacher, J. G., Jaroszynski, D. A., Kaluza, M. C., Hidding, B., Kiselev, S., Heathcote, R., Foster, P. S., Neely, D., Divall, E. J., Hooker, C. J., Smith, J. M., Ertel, K., Langley, A. J., Norreys, P., Collier, J. L. & Karsch, S. (2010). Electron bunch length measurements from laser-accelerated electrons using single-shot THz time-domain interferometry, *Phys. Rev. Lett.* 104: 084802.

Decker, C. D., Mori, W. B. & Katsouleas, T. (1994). Particle-in-cell simulations of Raman forward scattering from short-pulse high-intensity lasers, *Phys. Rev. E* 50: R3338–R3341.

Ebrahim, N. A. (1994). Optical mixing of laser light in a plasma and electron acceleration by relativistic electron plasma waves, *J. Appl. Phys.* 76: 7645–7647.

Esarey, E., Hubbard, R. F., Leemans, W. P., Ting, A. & Sprangle, P. (1997). Electron injection into plasma wakefields by colliding laser pulses, *Phys. Rev. Lett.* 79: 2682–2685.

Esarey, E., Schroeder, C. B. & Leemans, W. P. (2009). Physics of laser-driven plasma-based electron accelerators, *Rev. Mod. Phys.* 81: 1229–1285.

Esarey, E., Sprangle, P., Krall, J. & Ting, A. (1996). Overview of plasma-based accelerator concepts, *IEEE Trans. Plasma Sci.* 24: 252–288.

Faure, J., Glinec, Y., Pukhov, A., Kiselev, S., Gordienko, S., Lefebvre, E., Rousseau, J. P., Burgy, F. & Malka, V. (2004). A laser-plasma accelerator producing monoenergetic electron beams, *Nature* 431: 541–544.

Faure, J., Rechatin, C., Norlin, A., Lifschitz, A., Glinec, Y. & Malka, V. (2006). Controlled injection and acceleration of electrons in plasma wakefields by colliding laser pulses, *Nature* 444: 737–739.

Fuchs, M., Weingartner, R., Popp, A., Major, Z., Becker, S., Osterhoff, J., Cortrie, I., Zeitler, B., Hörlein, R., Tsakiris, G. D., Schramm, U., Rowlands-Rees, T. P., Hooker, S. M., Habs, D., Krausz, F., Karsch, S. & Gruener, F. (2009). Laser-driven soft-x-ray undulator source, *Nature Phys.* 5: 826–829.

Gahn, C., Tsakiris, G. D., Pukhov, A., Meyer-ter Vehn, J., Pretzler, G., Thirolf, P., Habs, D. & Witte, K. J. (1999). Multi-MeV electron beam generation by direct laser acceleration in high-density plasma channels, *Phys. Rev. Lett.* 83: 4772–4775.

Geddes, C. G. R., Tóth, C., van Tilborg, J., Esarey, E., Schroeder, C. B., Bruhwiler, D., Nieter, C., Cary, J. & Leemans, W. P. (2004). High-quality electron beams from a laser wakefield accelerator using plasma-channel guiding, *Nature* 431: 538–541.

Geissler, M., Schreiber, J. & ter Vehn, J. M. (2006). Bubble acceleration of electrons with few-cycle laser pulses, *New J. Phys.* 8: 186.

Glinec, Y., Faure, J., Norlin, A., Pukhov, A. & Malka, V. (2007). Observation of fine structures in laser-driven electron beams using coherent transition radiation, *Phys. Rev. Lett.* 98: 194801.

Gordienko, S. & Pukhov, A. (2005). Scalings for ultrarelativistic laser plasmas and quasimonoenergetic electrons, *Phys. Plasmas* 12: 043109.

Hafz, N. A. M., Jeong, T. M., Choi, I. W., Lee, S. K., Pae, K. H., Kulagin, V. V., Sung, J. H., Yu, T. J., Hong, K.-H., Hosokai, T., Cary, J. R., Ko, D.-K. & Lee, J. (2008). Stable generation of GeV-class electron beams from self-guided laser-plasma channels, *Nature Photon.* 2: 571–577.

Hidding, B., Amthor, K.-U., Liesfeld, B., Schwoerer, H., Karsch, S., Geissler, M., Veisz, L., Schmid, K., Gallacher, J. G., Jamison, S. P., Jaroszynski, D., Pretzler, G. & Sauerbrey, R. (2006). Generation of quasimonoenergetic electron bunches with 80-fs laser pulses, *Phys. Rev. Lett.* 96: 105004.

Hosokai, T., Kinoshita, K., Ohkubo, T., Maekawa, A., Uesaka, M., Zhidkov, A., Yamazaki, A., Kotaki, H., Kando, M., Nakajima, K., Bulanov, S. V., Tomassini, P., Giulietti, A. & Giulietti, D. (2006). Observation of strong correlation between quasimonoenergetic electron beam generation by laser wakefield and laser guiding inside a preplasma cavity, *Phys. Rev. E* 73: 036407.

Hosokai, T., Kinoshita, K., Zhidkov, A., Maekawa, A., Yamazaki, A. & Uesaka, M. (2006). Effect of external static magnetic field on the emittance and total charge of electron beams generated by laser-wakefield acceleration, *Phys. Rev. Lett.* 97: 075004.

Hsieh, C.-T., Huang, C.-M., Chang, C.-L., Ho, Y.-C., Chen, Y.-S., Lin, J.-Y., Wang, J. & Chen, S.-Y. (2006). Tomography of injection and acceleration of monoenergetic electrons in a laser-wakefield accelerator, *Phys. Rev. Lett.* 96: 095001.

Ikeura-Sekiguchi, H., Kuroda, R., Yasumoto, M., Toyokawa, H., Koike, M., Yamada, K., Sakai, F., Mori, K., Maruyama, K., Oka, H. & Kimata, T. (2008). In-line phase-contrast imaging of a biological specimen using a compact laser-Compton scattering-based x-ray source, *Appl. Phys. Lett.* 92: 131107.

Joshi, C., Mori, W. B., Katsouleas, T., Dawson, J. M., Kindel, J. M. & Forslund, D. W. (1984). Ultrahigh gradient particle-acceleration by intense laser-driven plasma-density waves, *Nature* 311: 525–529.

Kameshima, T., Hong, W., Sugiyama, K., Wen, X., Wu, Y., Tang, C., Zhu, Q., Gu, Y., Zhang, B., Peng, H., Kurokawa, S., Chen, L., Tajima, T., Kumita, T. & Nakajima, K. (2008). 0.56 GeV laser electron acceleration in ablative-capillary-discharge plasma channel, *Applied Physics Express* 1: 066001.

Kando, M., Fukuda, Y., Pirozhkov, A. S., Ma, J., Daito, I., Chen, L.-M., Esirkepov, T. Z., Ogura, K., Homma, T., Hayashi, Y., Kotaki, H., Sagisaka, A., Mori, M., Koga, J. K., Daido, H., Bulanov, S. V., Kimura, T., Kato, Y. & Tajima, T. (2007). Demonstration of laser-frequency upshift by electron-density modulations in a plasma wakefield, *Phys. Rev. Lett.* 99: 135001.

Kando, M., Pirozhkov, A. S., Kawase, K., Esirkepov, T. Z., Fukuda, Y., Kiriyama, H., Okada, H., Daito, I., Kameshima, T., Hayashi, Y., Kotaki, H., Mori, M., Koga, J. K., Daido, H., Faenov, A. Y., Pikuz, T., Ma, J., Chen, L.-M., Ragozin, E. N., Kawachi, T., Kato, Y., Tajima, T. & Bulanov, S. V. (2009). Enhancement of photon number reflected by the relativistic flying mirror, *Phys. Rev. Lett.* 103: 235003.

Karsch, S., Osterhoff, J., Popp, A., Rowlands-Rees, T. P., Major, Z., Fuchs, M., Marx, B., Hörlein, R., Schmid, K., Veisz, L., Becker, S., Schramm, U., Hidding, B., Pretzler, G., Habs, D., Gruner, F., Krausz, F. & Hooker, S. M. (2007). GeV-scale electron acceleration in a gas-filled capillary discharge waveguide, *New J. Phys.* 9: 415.

Kitagawa, Y., Matsumoto, T., Minamihata, T., Sawai, K., Matsuo, K., Mima, K., Nishihara, K., Azechi, H., Tanaka, K. A., Takabe, H. & Nakai, S. (1992). Beat-wave excitation of plasma wave and observation of accelerated electrons, *Phys. Rev. Lett.* 68: 48–51.

Kitagawa, Y., Sentoku, Y., Akamatsu, S., Sakamoto, W., Kodama, R., Tanaka, K. A., Azumi, K., Norimatsu, T., Matsuoka, T., Fujita, H. & Yoshida, H. (2004). Electron acceleration in an ultraintense-laser-illuminated capillary, *Phys. Rev. Lett.* 92: 205002.

Kostyukov, I., Pukhov, A. & Kiselev, S. (2004). Phenomenological theory of laser-plasma interaction in "bubble" regime, *Phys. Plasmas* 11: 5256–5264.

Kotaki, H., Daito, I., Kando, M., Hayashi, Y., Kawase, K., Kameshima, T., Fukuda, Y., Homma, T., Ma, J., Chen, L.-M., Esirkepov, T. Z., Pirozhkov, A. S., Koga, J. K., Faenov, A., Pikuz, T., Kiriyama, H., Okada, H., Shimomura, T., Nakai, Y., Tanoue, M., Sasao, H., Wakai, D., Matsuura, H., Kondo, S., Kanazawa, S., Sugiyama, A., Daido, H. & Bulanov, S. V. (2009). Electron optical injection with head-on and countercrossing colliding laser pulses, *Phys. Rev. Lett.* 103: 194803.

Kotaki, H., Masuda, S., Kando, M., Koga, J. K. & Nakajima, K. (2004). Head-on injection of a high quality electron beam by the interaction of two laser pulses, *Phys. Plasmas* 11: 3296–3302.

Leemans, W. P., Nagler, B., Gonsalves, A. J., Tóth, C., Nakamura, K., Geddes, C. G. R., Esarey, E., Schroeder, C. B. & Hooker, S. M. (2006). Gev electron beams from a centimetre-scale accelerator, *Nature Phys.* 2: 696–699.

Lu, W., Tzoufras, M., Joshi, C., Tsung, F. S., Mori, W. B., Vieira, J., Fonseca, R. A. & Silva, L. O. (2007). Generating multi-gev electron bunches using single stage laser wakefield acceleration in a 3D nonlinear regime, *Phys. Rev. ST Accel. Beams* 10: 061301.

Lundh, O., Lim, J., Rechatin, C., Ammoura, L., Ben-Ismail, A., Davoine, X., Gallot, G., Goddet, J.-P., Lefebvre, E., Malka, V. & Faure, J. (2011). Few femtosecond, few kiloampere electron bunch produced by a laser-plasma accelerator, *Nature Phys.* 7: 219–222.

Maksimchuk, A., Reed, S., Naumova, N., Chvykov, V., Hou, B., Kalintchenko, G., Matsuoka, T., Nees, J., Rousseau, P., Mourou, G. & Yanovsky, V. (2007). Energy scaling of quasi-monoenergetic electron beams from laser wakefields driven by 40-TW ultra-short pulses, *Appl. Phys. B* 89: 201–207.

Malka, V., Fritzler, S., Lefebvre, E., Aleonard, M.-M., Burgy, F., Chambaret, J.-P., Chemin, J.-F., Krushelnick, K., Malka, G., Mangles, S. P. D., Najmudin, Z., Pittman, M., Rousseau, J.-P., Scheurer, J.-N., Walton, B. & Dangor, A. E. (2002). Electron acceleration by a wake field forced by an intense ultrashort laser pulse, *Science* 298: 1596–1600.

Mangles, S. P. D., Murphy, C. D., Najmudin, Z., Thomas, A. G. R., Collier, J. L., Dangor, A. E., Divall, E. J., Foster, P. S., Gallacher, J. G., Hooker, C. J., Jaroszynski, D. A., Langley, A. J., Mori, W. B., Norreys, P. A., Tsung, F. S., Viskup, R., Walton, B. R. & Krushelnick,

K. (2004). Monoenergetic beams of relativistic electrons from intense laser-plasma interactions, *Nature* 431: 535–538.

Mangles, S. P. D., Thomas, A. G. R., Lundh, O., Lindau, F., Kaluza, M. C., Persson, A., Wahlström, C.-G., Krushelnick, K. & Najmudin, Z. (2007). On the stability of laser wakefield electron accelerators in the monoenergetic regime, *Phys. Plasmas* 14: 056702.

Masuda, S. & Miura, E. (2008). Generation of quasi-monoenergetic electron beams with high charge by laser-driven plasma-based acceleration, *Appl. Phys. Express* 1: 086002.

Masuda, S. & Miura, E. (2009). Generation and analysis of quasimonoenergetic electron beams by laser-plasma interaction in transitional region from the self-modulated laser wakefield to bubble acceleration regime, *Phys. Plasmas* 16: 093105.

Masuda, S. & Miura, E. (2010). Effect of femtosecond prepulse with threshold intensity for optical field ionization on electron acceleration and propagation of intense laser pulse in plasma, *Jpn. J. Appl. Phys.* 49: 096401.

Masuda, S., Miura, E., Koyama, K. & Kato, S. (2008). Absolute calibration of an electron spectrometer using high energy electrons produced by the laser-plasma interaction, *Rev. Sci. Instrum.* 79: 083301.

Masuda, S., Miura, E., Koyama, K., Kato, S., Adachi, M., Watanabe, T., Torii, K. & Tanimoto, M. (2007). Energy scaling of monoenergetic electron beams generated by the laser-driven plasma based accelerator, *Phys. Plasmas* 14: 023103.

McGuffey, C., Thomas, A. G. R., Schumaker, W., Matsuoka, T., Chvykov, V., Dollar, F. J., Kalintchenko, G., Yanovsky, V., Maksimchuk, A., Krushelnick, K., Bychenkov, V. Y., Glazyrin, I. V. & Karpeev, A. V. (2010). Ionization induced trapping in a laser wakefield accelerator, *Phys. Rev. Lett.* 104: 025004.

Miura, E., Ishii, S., Tanaka, K., Kuroda, R. & Toyokawa, H. (2011). X-ray generation via laser compton scattering by laser-accelerated electron beam, *Proceedings of International Conference on Physics in Intense Fields PIF2010*, pp. 159–161.
URL: *http://ccdb4fs.kek.jp/tiff/2010/1025/1025013.pdf*

Miura, E., Koyama, K., Kato, S., Saito, N., Adachi, M., Kawada, Y., Nakamura, T. & Tanimoto, M. (2005). Demonstration of quasi-monoenergetic electron-beam generation in laser-driven plasma acceleration, *Appl. Phys. Lett.* 86: 251501.

Miura, E. & Masuda, S. (2009). Stable generation of quasi-monoenergetic electron beams with laser-driven plasma-based acceleration by suppressing nanosecond prepulse, *Appl. Phys. Express* 2: 126003.

Modena, A., Najmudin, Z., Dangor, A. E., Clayton, C. E., Marsh, K. A., Joshi, C., Malka, V., Darrow, C. B., Danson, C., Neely, D. & Walsh, F. N. (1995). Electron acceleration from the breaking of relativistic plasma-waves, *Nature* 377: 606–608.

Mori, M., Kando, M., Daito, I., Kotaki, H., Hayashi, Y., Yamazaki, A., Ogura, K., Sagisaka, A., Koga, J., Nakajima, K., Daido, H., Bulanov, S. & Kimura, T. (2006). Transverse dynamics and energy tuning of fast electrons generated in sub-relativistic intensity laser pulse interaction with plasmas, *Phys. Lett. A* 356: 146 – 151.

Mori, M., Kondo, K., Mizuta, Y., Kando, M., Kotaki, H., Nishiuchi, M., Kado, M., Pirozhkov, A. S., Ogura, K., Sugiyama, H., Bulanov, S. V., Tanaka, K. A., Nishimura, H. & Daido, H. (2009). Generation of stable and low-divergence 10-MeV quasimonoenergetic electron bunch using argon gas jet, *Phys. Rev. ST Accel. Beams* 12: 082801.

Mori, Y., Sentoku, Y., Kondo, K., Tsuji, K., Nakanii, N., Fukumochi, S., Kashihara, M., Kimura, K., Takeda, K., Tanaka, K. A., Norimatsu, T., Tanimoto, T., Nakamura, H., Tampo, M., Kodama, R., Miura, E., Mima, K. & Kitagawa, Y. (2009). Autoinjection of electrons into a wake field using a capillary with attached cone, *Phys. Plasmas* 16: 123103.

Nakajima, K., Fisher, D., Kawakubo, T., Nakanishi, H., Ogata, A., Kato, Y., Kitagawa, Y., Kodama, R., Mima, K., Shiraga, H., Suzuki, K., Yamakawa, K., Zhang, T., Sakawa, Y., Shoji, T., Nishida, Y., Yugami, N., Downer, M. & Tajima, T. (1995). Observation of ultrahigh gradient electron acceleration by a self-modulated intense short laser pulse, *Phys. Rev. Lett.* 74: 4428–4431.

Nakanii, N., Kondo, K., Kuramitsu, Y., Mori, Y., Miura, E., Tsuji, K., Kimura, K., Fukumochi, S., Kashihara, M., Tanimoto, T., Nakamura, H., Ishikura, T., Takeda, K., Tampo, M., Takabe, H., Kodama, R., Kitagawa, Y., Mima, K. & Tanaka, K. A. (2008). Spectrum modulation of relativistic electrons by laser wakefield, *Appl. Phys. Lett.* 93: 081501.

Ohkubo, T., Maekawa, A., Tsujii, R., Hosokai, T., Kinoshita, K., Kobayashi, K., Uesaka, M., Zhidkov, A., Nemoto, K., Kondo, Y. & Shibata, Y. (2007). Temporal characteristics of monoenergetic electron beams generated by the laser wakefield acceleration, *Phys. Rev. ST Accel. Beams* 10: 031301.

Osterhoff, J., Popp, A., Major, Z., Marx, B., Rowlands-Rees, T. P., Fuchs, M., Geissler, M., Hörlein, R., Hidding, B., Becker, S., Peralta, E. A., Schramm, U., Grüner, F., Habs, D., Krausz, F., Hooker, S. M. & Karsch, S. (2008). Generation of stable, low-divergence electron beams by laser-wakefield acceleration in a steady-state-flow gas cell, *Phys. Rev. Lett.* 101: 085002.

Pak, A., Marsh, K. A., Martins, S. F., Lu, W., Mori, W. B. & Joshi, C. (2010). Injection and trapping of tunnel-ionized electrons into laser-produced wakes, *Phys. Rev. Lett.* 104: 025003.

Perry, M. D., Pennington, D., Stuart, B. C., Tietbohl, G., Britten, J. A., Brown, C., Herman, S., Golick, B., Kartz, M., Miller, J., Powell, H. T., Vergino, M. & Yanovsky, V. (1999). Petawatt laser pulses, *Opt. Lett.* 24: 160–162.

Phuoc, K. T., Fitour, R., Tafzi, A., Garl, T., Artemiev, N., Shah, R., Albert, F., Boschetto, D., Rousse, A., Kim, D.-E., Pukhov, A., Seredov, V. & Kostyukov, I. (2007). Demonstration of the ultrafast nature of laser produced betatron radiation, *Phys. Plasmas* 14: 080701.

Pukhov, A. & Meyer-ter Vehn, J. (2002). Laser wake field acceleration: the highly non-linear broken-wave regime, *Appl. Phys. B* 74: 355–361.

Rousse, A., Phuoc, K. T., Shah, R., Pukhov, A., Lefebvre, E., Malka, V., Kiselev, S., Burgy, F., Rousseau, J.-P., Umstadter, D. & Hulin, D. (2004). Production of a keV x-ray beam from synchrotron radiation in relativistic laser-plasma interaction, *Phys. Rev. Lett.* 93: 135005.

Rowlands-Rees, T. P., Kamperidis, C., Kneip, S., Gonsalves, A. J., Mangles, S. P. D., Gallacher, J. G., Brunetti, E., Ibbotson, T., Murphy, C. D., Foster, P. S., Streeter, M. J. V., Budde, F., Norreys, P. A., Jaroszynski, D. A., Krushelnick, K., Najmudin, Z. & Hooker, S. M. (2008). Laser-driven acceleration of electrons in a partially ionized plasma channel, *Phys. Rev. Lett.* 100: 105005.

Schlenvoigt, H. P., Haupt, K., Debus, A., Budde, F., Jäckel, O., Pfotenhauer, S., Schwoerer, H., Rohwer, E., Gallacher, J. G., Brunetti, E., Shanks, R. P., Wiggins, S. M. & Jaroszynski, D. A. (2008). A compact synchrotron radiation source driven by a laser-plasma wakefield accelerator, *Nature Phys.* 4: 130–133.

Schoenlein, R. W., Leemans, W. P., Chin, A. H., Volfbeyn, P., Glover, T. E., Balling, P., Zolotorev, M., Kim, K.-J., Chattopadhyay, S. & Shank, C. V. (1996). Femtosecond x-ray pulses at 0.4 Å generated by 90° Thomson scattering: A tool for probing the structural dynamics of materials, *Science* 274: 236–238.

Schwoerer, H., Liesfeld, B., Schlenvoigt, H.-P., Amthor, K.-U. & Sauerbrey, R. (2006). Thomson-backscattered x rays from laser-accelerated electrons, *Phys. Rev. Lett.* 96: 014802.

Strickland, D. & Mourou, G. (1985). Compression of amplified chirped optical pulses, *Opt. Commun.* 56: 219–221.

Tajima, T. & Dawson, J. M. (1979). Laser electron accelerator, *Phys. Rev. Lett.* 43: 267–270.

Tanaka, K. A., Yabuuchi, T., Sato, T., Kodama, R., Kitagawa, Y., Takahashi, T., Ikeda, T., Honda, Y. & Okuda, S. (2005). Calibration of imaging plate for high energy electron spectrometer, *Rev. Sci. Instrum.* 76: 013507.

Umstadter, D., Chen, S.-Y., Maksimchuk, A., Mourou, G. & Wagner, R. (1996). Nonlinear optics in relativistic plasmas and laser wake field acceleration of electrons, *Science* 273: 472–475.

Umstadter, D., Kim, J. K. & Dodd, E. (1996). Laser injection of ultrashort electron pulses into wakefield plasma waves, *Phys. Rev. Lett.* 76: 2073–2076.

van Tilborg, J., Schroeder, C. B., Filip, C. V., Tóth, C., Geddes, C. G. R., Fubiani, G., Huber, R., Kaindl, R. A., Esarey, E. & Leemans, W. P. (2006). Temporal characterization of femtosecond laser-plasma-accelerated electron bunches using terahertz radiation, *Phys. Rev. Lett.* 96: 014801.

Verluise, F., Laude, V., Cheng, Z., Spielmann, C. & Tournois, P. (2000). Amplitude and phase control of ultrashort pulses by use of an acousto-optic programmable dispersive filter: pulse compression and shaping, *Opt. Lett.* 25: 575–577.

Yamazaki, A., Kotaki, H., Daito, I., Kando, M., Bulanov, S. V., Esirkepov, T. Z., Kondo, S., Kanazawa, S., Homma, T., Nakajima, K., Oishi, Y., Nayuki, T., Fujii, T. & Nemoto, K. (2005). Quasi-monoenergetic electron beam generation during laser pulse interaction with very low density plasmas, *Phys. Plasmas* 12: 093101.

Yorozu, M., Yang, J., Okada, Y., Yanagida, T., Sakai, F., Takasago, K., Ito, S. & Endo, A. (2002). Fluctuation of femtosecond x-ray pulses generated by a laser-compton scheme, *Appl. Phys. B* 74: 327–331.

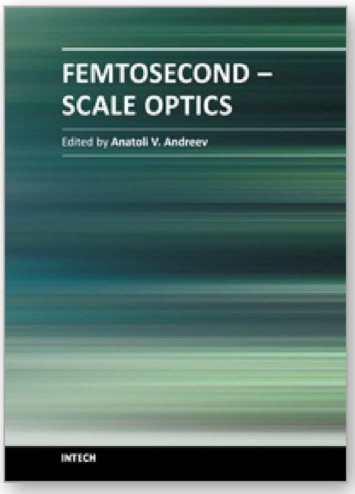

Femtosecond-Scale Optics
Edited by Prof. Anatoly Andreev

ISBN 978-953-307-769-7
Hard cover, 434 pages
Publisher InTech
Published online 14, November, 2011
Published in print edition November, 2011

With progress in ultrashort ultraintense laser technologies the peak power of a laser pulse increases year by year. These new instruments accessible to a large community of researchers revolutionized experiments in nonlinear optics because when laser pulse intensity exceeds or even approaches intra-atomic field strength the new physical picture of light-matter interaction appears. Laser radiation is efficiently transformed into fluxes of charged or neutral particles and the very wide band of electromagnetic emission (from THz up to x-rays) is observed. The traditional phenomena of nonlinear optics as harmonic generation, self-focusing, ionization, etc, demonstrate the drastically different dependency on the laser pulse intensity in contrast the well known rules. This field of researches is in rapid progress now. The presented papers provide a description of recent developments and original results obtained by authors in some specific areas of this very wide scientific field. We hope that the Volume will be of interest for those specialized in the subject of laser-matter interactions.

InTech Europe
University Campus STeP Ri
Slavka Krautzeka 83/A
51000 Rijeka, Croatia
Phone: +385 (51) 770 447
Fax: +385 (51) 686 166
www.intechopen.com

InTech China
Unit 405, Office Block, Hotel Equatorial Shanghai
No.65, Yan An Road (West), Shanghai, 200040, China
中国上海市延安西路65号上海国际贵都大饭店办公楼405单元
Phone: +86-21-62489820
Fax: +86-21-62489821